Exploring various corona geometries and their emissivity profiles

by

Adam Gonzalez

A Thesis Submitted to
Saint Mary's University, Halifax, Nova Scotia
in Partial Fulfillment of the Requirements for
the Degree of Master of Science in Astronomy
(Department of Astronomy and Physics)

2017, Halifax, Nova Scotia

Approved: Dr. Luigi Gallo

(Supervisor)

Approved: Dr. Robert Thacker

(Examiner)

Approved: Dr. Marcin Sawicki

(Examiner)

Date: April 24, 2017.

Acknowledgements

I would like to thank my supervisor Dr. Luigi Gallo as well as Dr. Daniel Wilkins for providing the support and considerable patience necessary for me to complete the work presented within this thesis.

I would also like to extend this thanks to all of the faculty, staff, and other graduate students, especially Diego, Hannah, and Kirsten, for their many helpful insights and comments throughout the research and writing periods.

Contents

Sections of Chapter 1 and Chapters 2 – 7 are as they appear published in Gonzalez, A.G., Wilkins, D.R., & Gallo, L.C. 2017 submitted to MNRAS.

List of Figures

List of Tables

Abstract

Exploring various corona geometries and their emissivity profiles

by Adam Gonzalez

The differences in emissivity profiles produced by various corona geometries are explored via general relativistic ray tracing simulations in order to better understand the inner disc region of active galactic nuclei. Emissivity profiles produced by point sources are distinguishable from those produced by cylindrical slabs and spheroidal coronae, but are indistinguishable from profiles produced by conical geometries, requiring an analysis of reflection fraction to differentiate them. Beamed point and beamed conical sources exhibit differences most evident in the reflection fraction. For point sources a relationship for the measured reflection fraction with source height and velocity is determined. Simulating spectra from the emissivity profiles produced by the various geometries produce distinguishable differences that do not exceed 15 per cent in the most extreme cases. Emissivity profiles are found to be useful in distinguishing point source and extended geometries given high quality spectral data of extreme, bright sources over long exposure times.

April 24, 2017

Chapter 1

Introduction

1.1 Active Galactic Nuclei

Active galactic nuclei (AGN) are responsible for some of the most energetic and luminous X-ray phenomena in the Universe. These objects were first detailed by Seyfert (1943) as galaxies with nuclei far brighter than normal and possessing spectra with broad spectral lines. It has since been found that AGN are comprised of supermassive black holes (SMBHs) that range in mass from $\sim 10^6 - 10^9\,\mathrm{M}_\odot$. These massive objects and the environment in which they reside have been studied in great detail since Seyfert's discovery, though some fundamental aspects of AGN remain without a complete understanding.

Evidence suggests that a SMBH lies at the centre of every galaxy, as indicated by the stellar and gas kinematics in these regions (e.g. Schödel et al. 2002; Ghez et al. 2003). Those deemed active are found to be actively accreting surrounding material, emitting huge amounts of electromagnetic radiation in the process. Unlike other energetic sources in the

Universe that emit in short bursts, the accretion processes of SMBHs allow for AGN to be the most luminous continuous sources known. This emission covers a large portion of the electromagnetic spectrum ranging from radio waves up to and including gamma rays. Compared to normal galaxies, which have spectral energy distributions (SEDs) produced by starlight forming a black body shape, the SEDs of AGN are approximated by a power law across the wide range of wavelengths emitted by these objects, dropping off significantly at the longer (radio) wavelengths, as shown in Figure 1.1.

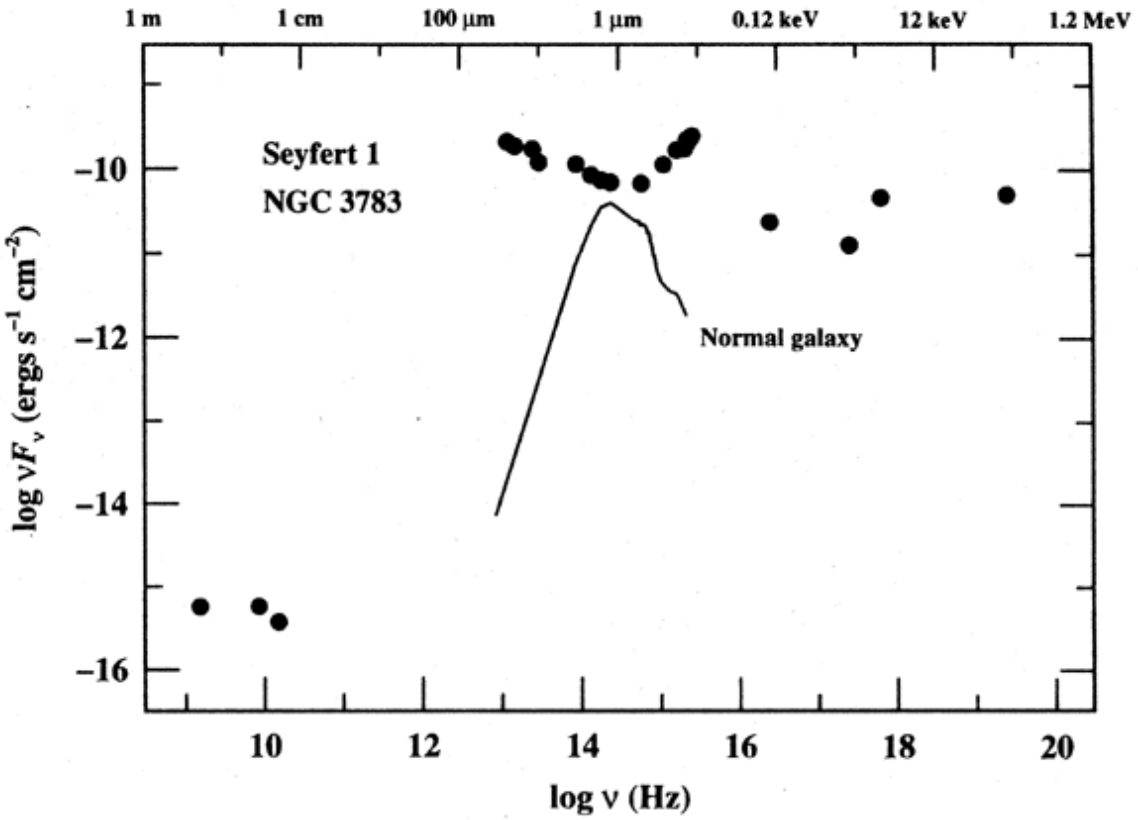

Figure 1.1: A comparison of the spectral energy distribution (SED) from a normal (spiral) galaxy to that of a Seyfert 1 AGN from radio to γ-ray wavelengths. Figure from Peterson (1997).

1.1.1 Components of AGN

The various components of AGN are responsible for the emission of electromagnetic radiation at a variety of wavelengths. Surrounding the black hole, providing material for the accretion process, is an optically thick, geometrically thin disc of gas as described by Shakura & Sunyaev (1973) that emits brightest in UV wavelengths. Above the black hole and accretion disc system resides the primary X-ray emitter, known as the corona, for which the exact geometry is an area of ongoing investigation. It is comprised of extremely hot electrons ($\gtrsim 10^9\,\mathrm{K}$) that have likely been liberated from the ionized material in the accretion disc. The formation of the corona is thought to be a result of the acceleration and confinement of energetic particles by magnetic fields anchored on the accretion disc (Galeev et al. 1979; Haardt & Maraschi 1991; Merloni & Fabian 2001). Its geometry is likely to be complex (e.g. patchy or collimated) (e.g. Wilkins & Gallo 2015a; Wilkins et al. 2015), extended over some part of the inner disc (e.g. Wilkins & Fabian 2012; henceforth WF12), and dynamic on various time scales (e.g. Gallo et al. 2015; Wilkins & Gallo 2015b).

All three of these components, the disc, corona, and black hole, lie within the central region of a dusty torus, through which low energy X-rays cannot penetrate because of the high column densities ($N_\mathrm{H} \sim 10^{24}\,\mathrm{cm}^{-2}$). Before encountering the dusty torus, however, emission from the central part of the AGN must pass through the broad-line region (BLR), which is responsible for the production of broad emission lines observed in AGN spectra. To produce these broad lines, velocities in the BLR must be $\sim 10^3 - 10^4\,\mathrm{km\,s}^{-1}$ and are attributed to winds coming off of the accretion disc (e.g Murray & Chiang 1997). On much

larger scales (e.g. host galaxy) exists the narrow-line region (NLR) from which the narrow lines in AGN spectra originate and exhibit velocities of $\sim 10^2 - 10^3\,\mathrm{km\,s^{-1}}$. The dynamics are likely originating from outflows. Current technologies are capable only of observing the much larger NLR, leaving the description of the BLR an open area of research.

1.1.2 Unification of AGN

The classification of AGN into a variety of subgroups is based on their physical and observational properties. One such classification system assigns Seyfert I to those AGN whose optical spectra contain both broad and narrow emission lines and Seyfert II to those that only exhibit broad lines. It has since been determined that the broad emission lines characteristic of Seyfert I galaxies and the lack thereof in Seyfert II objects is due to the viewing angle at which we observe these objects (e.g. Antonucci & Miller 1985; Antonucci 1993; Urry & Padovani 1995). By observing these systems edge-on (the normal vector of the accretion disc is perpendicular to our line of sight) the central regions of the AGN become obscured by the dusty torus, preventing the BLR from being observed. In the case of Seyfert I type AGN the object is viewed more face-on leaving the BLR visible producing both broad and narrow emission in their spectra. The situation is shown schematically in Figure 1.2. Other classifications exist based on, for example, the amount of radio emission produced by the AGN (radio loud versus radio quiet).

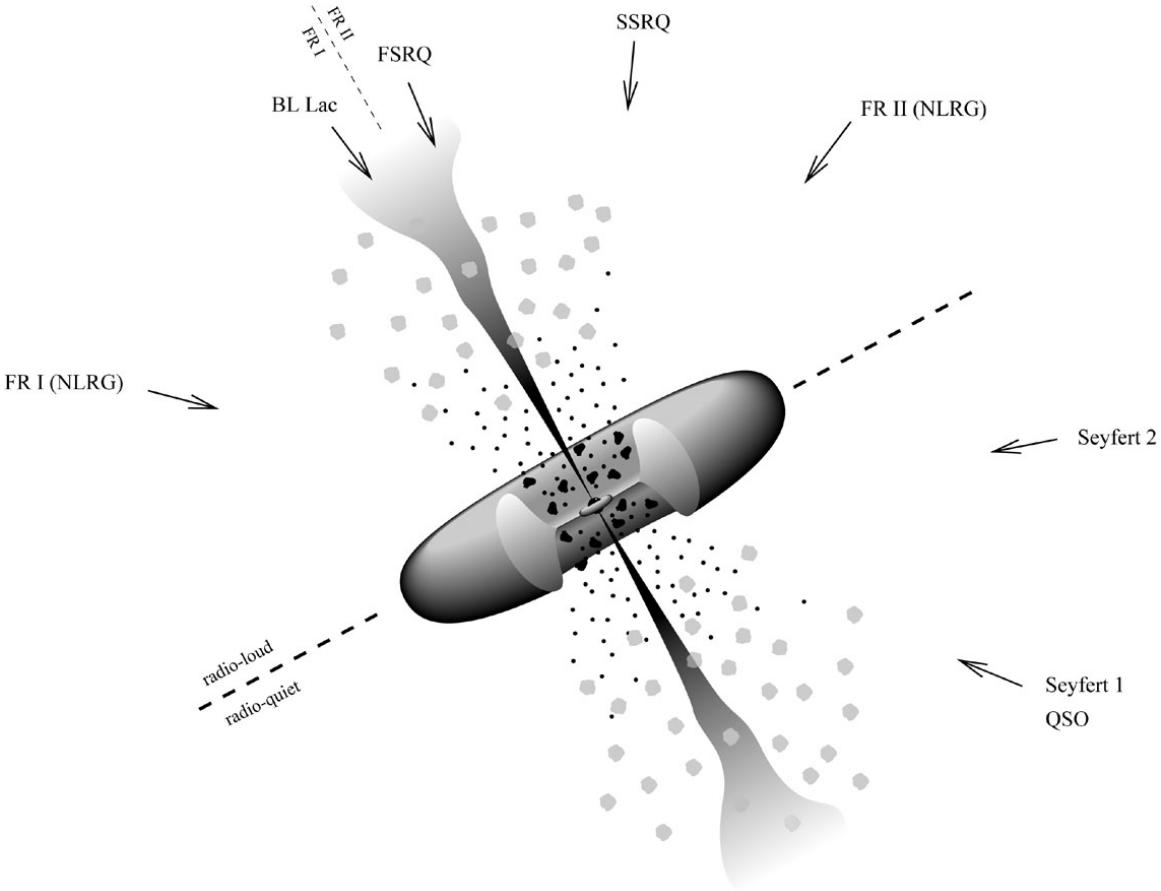

Figure 1.2: A schematic diagram detailing the inner region of AGN. The dusty torus that produces the distinction between Seyfert I and Seyfert II galaxies can be seen surrounding the broad-line region, accretion disc, and black hole. Components presented are not shown to scale. Figure from Torres (2003).

1.1.3 Broadband Spectrum

The broadband spectrum of AGN can be approximated by a power law across a large range of the electromagnetic spectrum, differing from the black body shape characteristic of normal galaxies (Figure 1.1). Notable features, however, exist in AGN spectra that deviate from the power law description as seen in Figure 1.3. All AGN produce radio wavelength radiation and significantly more than normal galaxies. However, this part of the spectrum

is much reduced in flux compared to the optical, UV, and X-ray bands even in those sources classified as being radio loud. Origin of the radio wavelength emission is attributed to non-thermal processes such as synchrotron radiation due to extended radio jets. Unlike radio emission, the infrared (IR) bump is thought to be thermal in origin, coming from re-emission of absorbed higher energy emission by warm dust grains in the torus. The Big Blue Bump is another deviation from the power law description in the optical / UV region of the spectrum stemming from UV emission by the accretion disc (discussed in greater detail in the following section) and has the shape of a modified black body. Both low- and high-energy X-rays comprise a small portion of the total luminosity emitted by AGN ($\sim 10\%$). The origin of this emisison will be discussed in further detail in the coming section, though importantly the information about the inner region of the AGN system encoded in the X-ray spectra is invaluable for gaining an understanding of these objects.

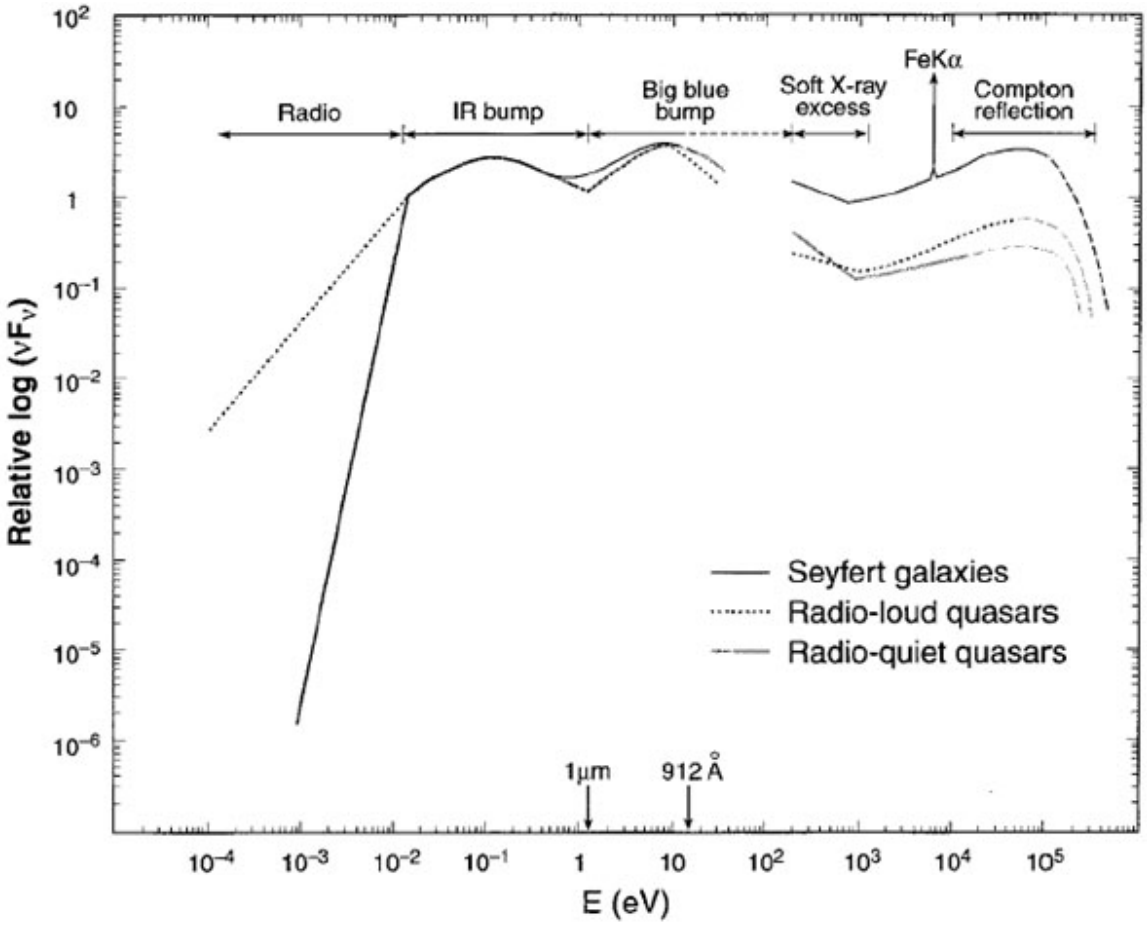

Figure 1.3: A comparison of the broadband SED for various AGN types. Segments of the SED based on wavelength range and feature type are also noted. Figure from Koratkar & Blaes (1999).

1.2 X-ray Spectrum of Type I AGN

Type I AGN (e.g. Seyfert I) provide an unobstructed view of the central region, making them ideal objects for which to study the X-ray properties of AGN. The X-ray spectrum itself is produced by two aforementioned central components: the accretion disc and corona. Of these two, only the disc emits its own intrinsic radiation produced by differential rotation and the viscosity of material in the disc. These processes heat the gaseous material comprising

the disc and transfer angular momentum from the inner radii to the outer portions of the disc, allowing the gas to fall inward toward the black hole. As a result, the disc radiates in the UV, producing thermal emission, some of which then goes on to interact with the corona. Inverse Compton scattering of these UV seed photons takes place in the hot sea of electrons above the disc, producing non-thermal X-ray emission. At this point in time the exact geometry of the corona remains unknown, though reverberation mapping studies reveal that it is likely compact and near the black hole (Fabian et al. 2009, 2013; Zoghbi et al. 2010).

Recent studies have also shown, however, that atmosphere-like coronae covering large portions of the accretion disc may also be suitable models for the geometry of the X-ray source (e.g. WF12, Wilkins & Gallo 2015b). Various examples of possible source geometries are shown in Figure 1.4. Regardless of the X-ray source geometry, the isotropic emission from the corona will be observed directly producing a power law component in AGN X-ray spectra. A portion of the X-rays will also go on to illuminate the accretion disc, producing the reflection spectrum (discussed in more detail in a following section). Thus, a two-component X-ray spectrum composed of a power law and reflection component produce the observed X-ray spectrum in AGN, which is shown schematically in Figure 1.5.

The power law turns over in both the UV and hard X-ray regimes. In the high-energy X-ray band the turnover is a result of the hot electrons comprising the corona no longer being able to scatter the seed photons to higher energies (i.e. an equilibrium between the photon and electron energies is reached). X-rays incident on the accretion disc will be absorbed (photoelectric absorption) and re-emitted by the gas in the disc (fluorescence) producing a

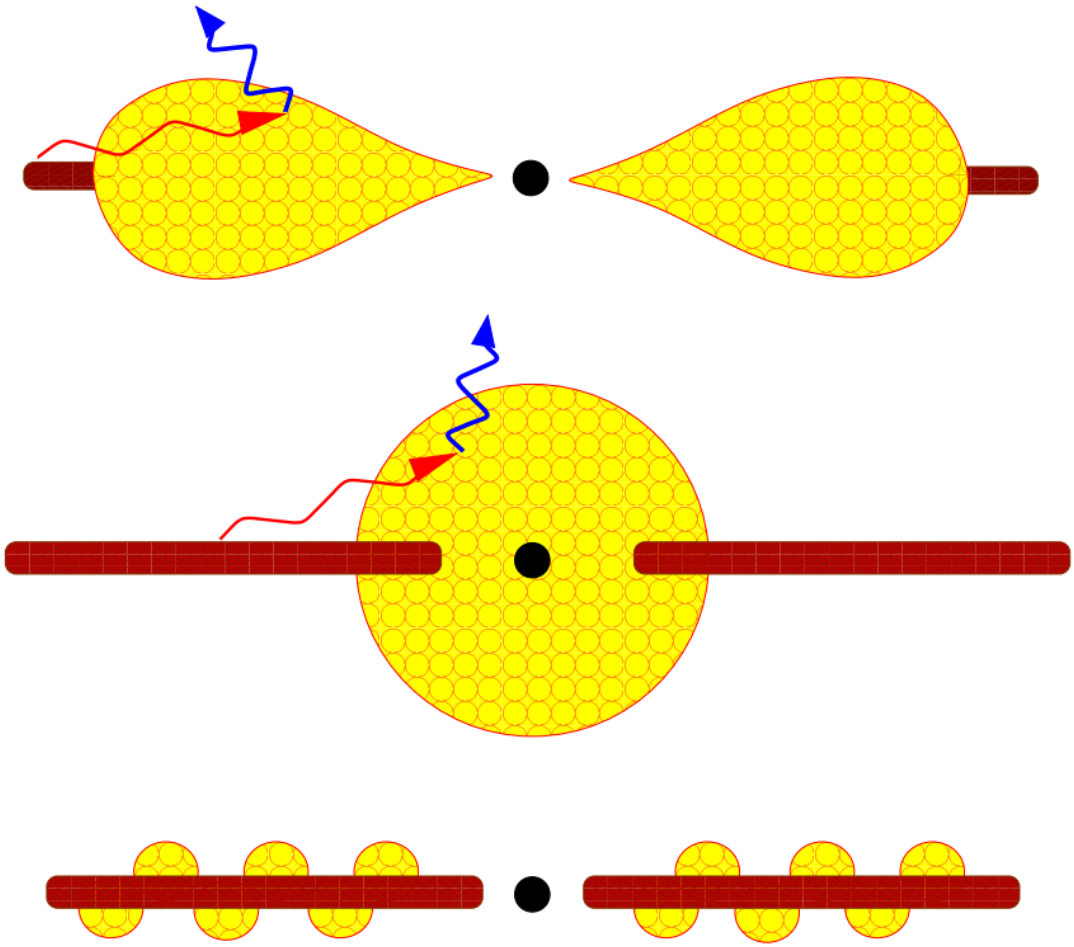

Figure 1.4: Schematic diagrams for the various possible corona geometries responsible for the X-ray emission in AGN. Ultra-violet seed photons form the disc are inverse Compton scattered in the corona producing X-rays. Figure from Reynolds & Nowak (2003).

variety of emission lines in the reflection spectrum. The most notable emission line in the X-ray band of AGN spectra is the Fe Kα line at 6.4 keV.

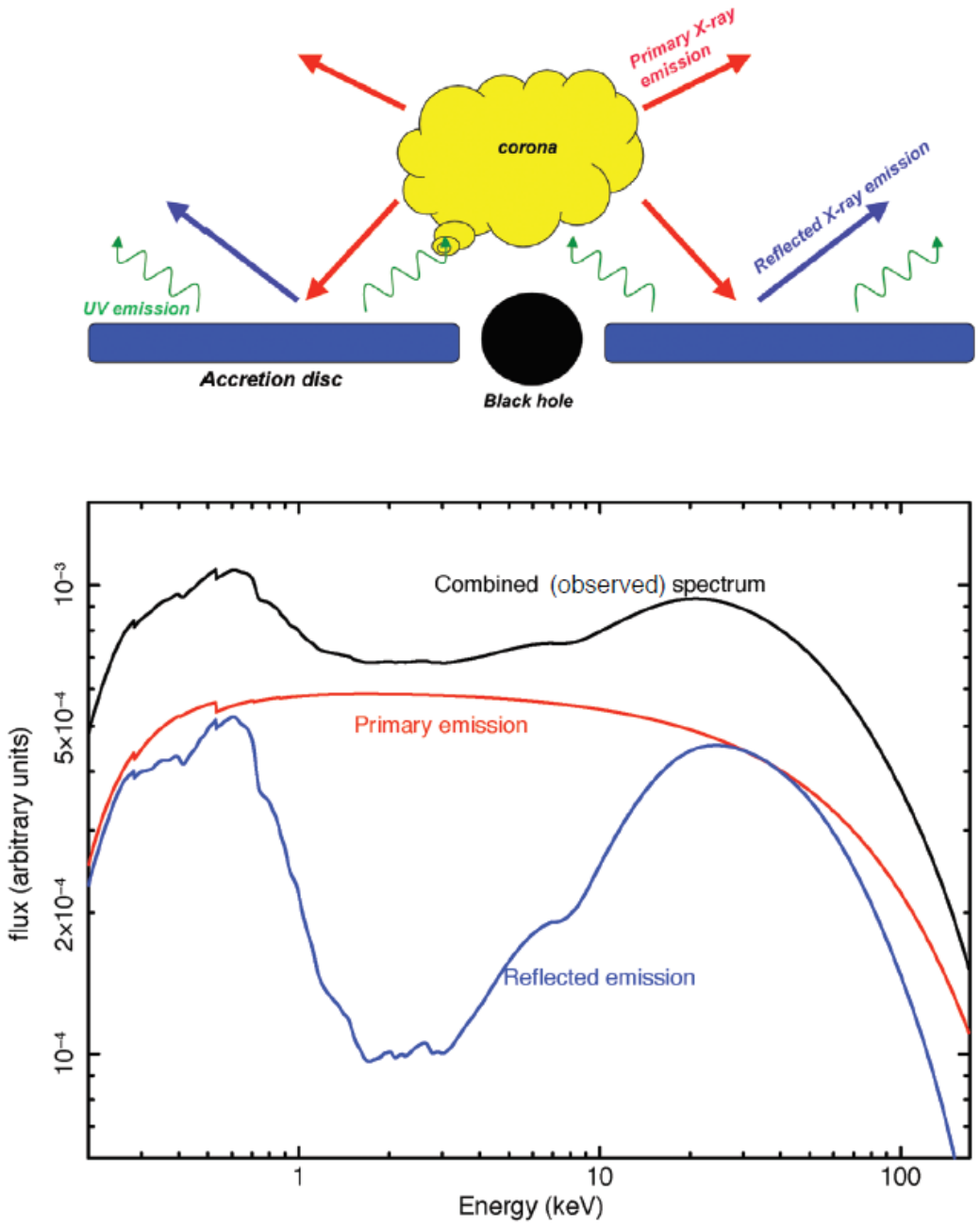

Figure 1.5: The top diagram shows how emission from the corona can either be observed directly or reflected off of the accretion disc to create the reflection spectrum. The bottom plot shows the primary X-ray emission from the corona and the reflection spectrum as well as the combined observed spectrum. Figure from Gallo (2011).

1.2.1 Absorption

The X-ray spectrum that we observe from AGN will have been attenuated by absorption processes due to the material along our line of sight to the object. There are many regions in which the intrinsic X-ray spectrum may be absorbed, processed, and re-emitted such as the BLR, NLR, dusty torus, dust and gas content in the host galaxy and Milky Way, to name a few. The differences between Seyfert I and Seyfert II galaxies, recall, are due to absorption effects by the dusty torus that obscure the BLR and prevent the soft X-ray emission from being observed. The spectra from objects with specifically warm absorption (i.e. optically thin, partially ionised gas) tend to exhibit more complex emission line features while spectra from sources suffering absorption from optically thick clouds (e.g. the torus) are typically harder (dominated by high-energy X-ray emission).

1.2.2 Distant Reflection

Emission from reflection peaks at energies $> 10\,\mathrm{keV}$ with the formation of the Compton hump. This hard X-ray tail of AGN spectra is thought to be a result of Compton scattering off of the accretion disc or some distant matter component (i.e. a cold gas) (Peterson 1997). In this scenario, photons emitted by an X-ray source above the accretion disc experience an inelastic scattering off of the low-energy electrons in the disc or cold gas.

1.2.3 Soft Excess

At lower energies (below $\sim 1\,\mathrm{keV}$) another excess is seen in the X-ray spectrum, this being known as the soft X-ray excess. The nature and origin of this spectral feature is hotly

debated, with evidence suggesting either blurred reflection (e.g. Crummy et al. 2006), absorption effects (e.g. Gierliński & Done 2004), or additional Comptonisation (e.g. Porquet et al. 2004) as explanations for its existence. The shape of the soft excess is that of a black body, and therefore some suggest that it may be the high-energy tail of the Big Blue Bump from the optical / UV range of the AGN spectrum (Malkan & Sargent 1982; Peterson 1997). With such an origin it is expected that a luminosity-temperature relationship for this emission would exist, but there is no such correlation (Porquet et al. 2004). The absence of a luminosity-temperature relationship indicates that the soft excess is not black body emission from the accretion disc, but may in fact be a result of atomic processes. Its shape may be due to blurring of emission lines resulting from the high velocities in the central region, smearing the lines together and forming the smooth shape seen.

1.3 Reflection Spectrum

1.3.1 Continuum & Emission Lines

Briefly discussed in a previous section, the reflection spectrum in AGN X-ray spectra is produced when X-ray emission from the corona illuminates and interacts with material in the accretion disc. High-energy X-rays will Compton scatter off of the cold material in the disc, thus producing the aforementioned Compton hump. Low-energy X-ray photons, however, will be absorbed by material in the disc, exciting the atoms which may then de-excite in one of two ways. The absorption of soft X-ray photons results in the excitation of an electron from, for example, the K ($n = 1$) shell. The first de-excitation path is known as

fluorescence and occurs as other electrons cascade down to fill the vacated level, generating an emission line in the process. The second de-excitation mechanism results in liberation of electrons in other shells of the atom (known as Auger de-excitation), however, this does not result in the production of a photon. The observed reflection spectrum in AGN contains emission lines according to the atomic species in the disc and as such is useful in determining composition of the accretion disc and provides valuable information on the incident X-ray spectrum that produced it.

The most prominent feature in the reflection spectrum is the presence of an emission line at 6.4 keV, which corresponds to Fe-Kα emission. The line itself is relatively isolated from the other emission lines in the reflection spectrum of AGN, which are mostly concentrated below $\sim$ 2 keV, as seen in Figure 1.6. Various physical parameters of the accretion disc, such as the ionisation level, temperature, composition, and abundance, may be determined based on the strength of emission lines in the reflection spectrum.

1.3.2 Disc Properties

The reflection spectrum may be modelled using what is known as a constant density model: a thin, cold, slab of constant density gas illuminated by an X-ray power law continuum (Ross & Fabian 1993). The emission lines observed in the reflection spectrum therefore depend on the ionisation level of this gas, which describes the rate at which photoionisation and recombination are balanced. The ionisation parameter, ξ, of the accretion disc gas is defined as $\xi(r) = 4\pi F_x(r)/n(r)$ where $F_x(r)$ is the X-ray flux received per unit area at radius r on the disc and $n(r)$ is the co-moving electron number density (ratio of the photoionisation

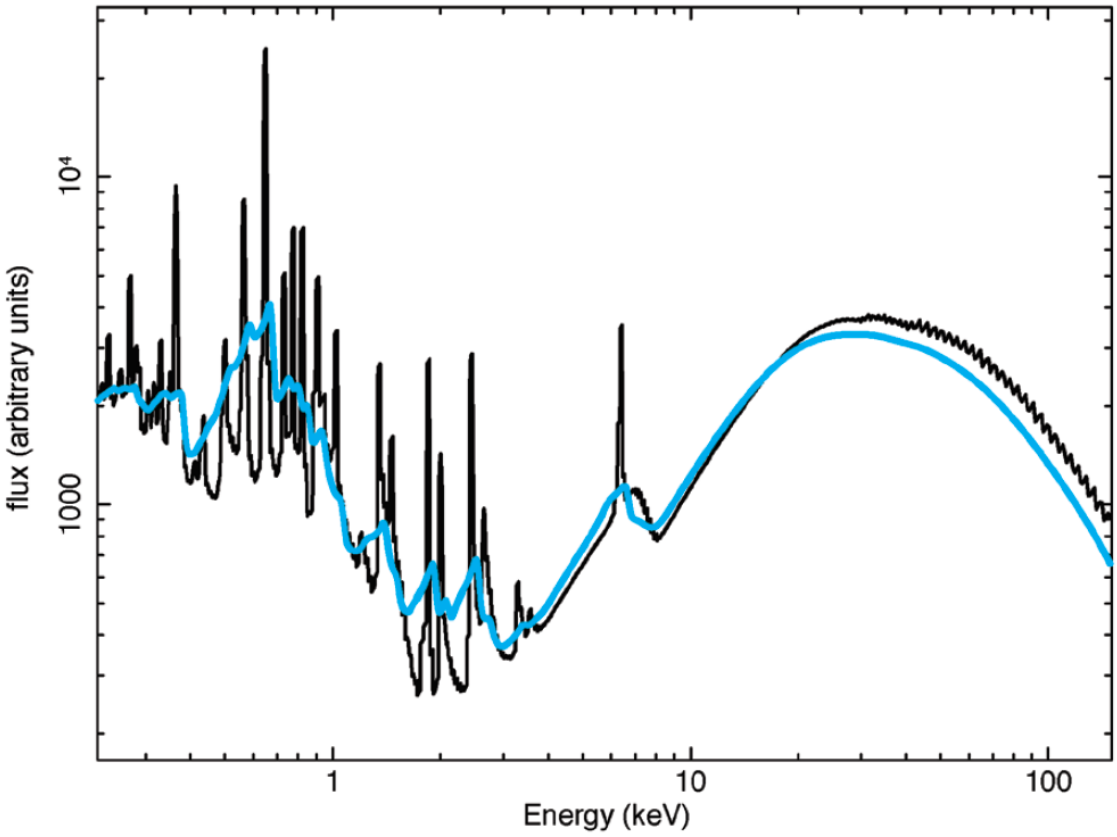

Figure 1.6: The reflection spectrum of an AGN is given by the black line. The blue line is the same reflection spectrum that has been modified due to blurring effects in the black hole environment. Figure from Gallo (2011).

to recombination rates) (Reynolds & Nowak 2003). The effect of ionisation parameter on the reflection spectrum can be seen in Figure 1.7. With increased ionisation the emission line features are dramatically reduced to point where at $\xi > 5000\,\mathrm{erg\,cm\,s^{-1}}$ the reflection spectrum becomes essentially featureless as the gas is completely ionised. In addition to ionisation, the abundance of different atomic species in the gas that makes up the accretion disc also determine what features we observe in the reflection spectrum. Increased iron abundance, for example, will greatly enhance the prominent Fe-Kα line while diminishing

the continuum due to iron absorption, as seen in Figure 1.8. Other effects on the shape and presence of emission lines observed in AGN reflection spectra are discussed in the next section.

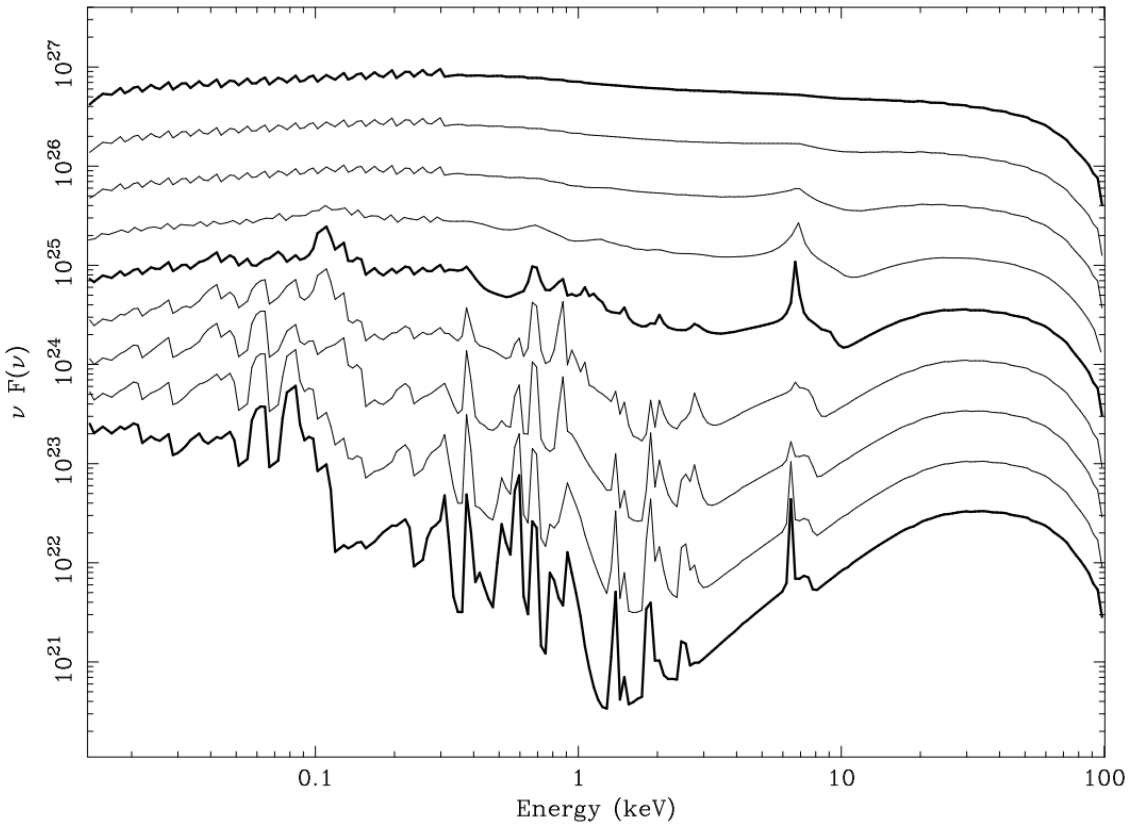

Figure 1.7: The effect of ionisation parameter on the reflection spectrum. From bottom to top $\log \xi$ ranges from 1.0 to 5.0 in increments of 0.5. Figure from Reynolds & Nowak (2003).

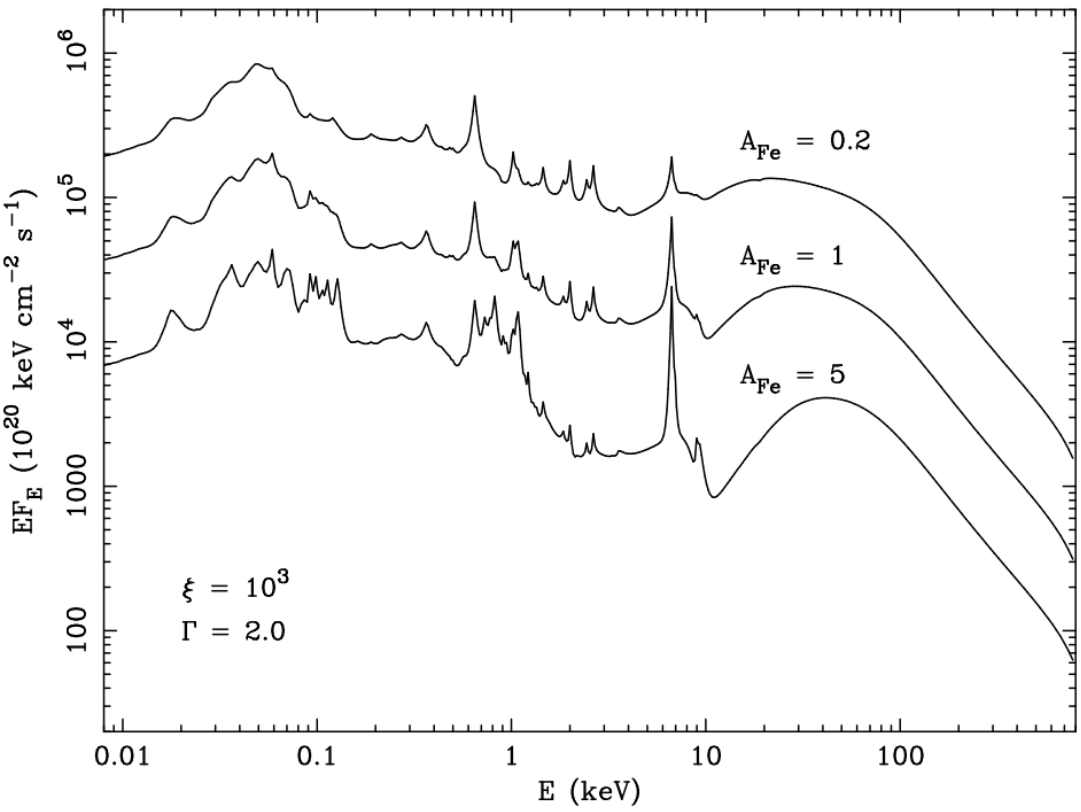

Figure 1.8: The effect of iron abundance (A_{Fe}) on the reflection spectrum. All three spectra have $\xi = 200\,\mathrm{erg\,cm\,s^{-1}}$ and $\Gamma = 2.0$. Figure from Ross & Fabian (2005).

1.4 Blurring Effects & Models

The emission lines present in reflection spectra of AGN are naturally narrow features that become broadened and blurred due to motion of the accretion disc and gravitational effects near the black hole (Figure 1.6). The blurring arises from multiple processes. Since the disc is rotating around the black hole, narrow emission lines will undergo Doppler broadening. A portion of the material is moving towards us, therefore resulting in a blueshift of the line energy producing a blue wing, while other material is moving away from us, producing

a red wing due to the redshift in emission line energy resulting in a characteristic double peaked line profile. Considering special relativistic effects for material near the black hole, which will be moving at speeds that are significant fractions of c, the double peaked profile becomes asymmetric. Material moving towards us is brightened due to beaming effects on the light emitted while material moving away from us suffers a dimming effect and is further redshifted due to the high velocity. Finally, including full general relativistic effects on material nearest the black hole, the emission line is made further asymmetric due to the immense gravitational potential that light must escape from at such a small distance from the event horizon. As light escapes from the potential well it loses energy, resulting in a greatly extended red wing and a reduced blue wing. The red wing is further extended to lower energies due to light emitted by material closest to the black hole losing more energy than light emitted by material in the disc further away. The observed emission line is therefore a summation of all the described broadening effects (Figure 1.9). Studying the emission lines in reflection spectra can therefore reveal information about dynamics of the black hole and accretion disc system.

1.4.1 Black Hole Spin

In addition to the motion in the accretion disc, the spin of the black hole, a, also has a significant effect on the shape of emission lines in the reflection spectrum of AGN. The dimensionless spin parameter is defined as $a_\star = Jc/GM^2$ where J is the angular momentum of the black hole and M is its mass. As the spin of the black hole is increased, material in the accretion disc is drawn nearer to the event horizon, the closest distance possible being where

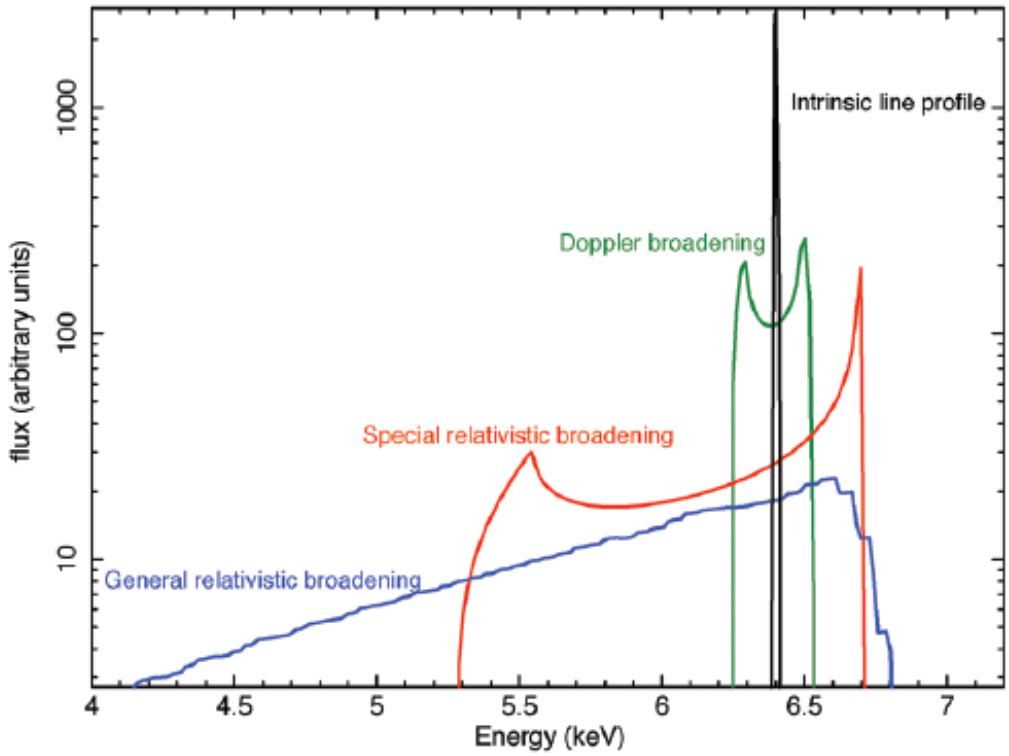

Figure 1.9: The effect of broadening on the intrinsically narrow iron line due to motion in the accretion disc and relativistic effects. Observed lines in AGN spectra are a summation of the three broadening mechanisms. Figure from Gallo (2011).

the innermost stable circular orbit (ISCO) can be completed. Higher spin values reduce the ISCO size, thus requiring photons emitted by material in this region to climb out of even deeper potential wells. This results in further loss of energy for such photons, extending the red wing of the emission line profiles. The case of a non-spinning ($a = 0$) Schwarzschild black hole finds emission lines, such as the Fe-Kα line, are as we would expect due to the motion effects described in the previous section. Increasing the spin up to a physical maximum ($a = 0.998$), known as a maximally spinning Kerr black hole, reduces the flux of the blue

wing of the line while increasing the flux measured in the red wing. This effect further broadens and blurs the emission line, as shown in Figure 1.10. By measuring the Fe-Kα line and its observed properties it is therefore possible to estimate the spin parameter of the black hole (e.g. Brenneman & Reynolds 2006).

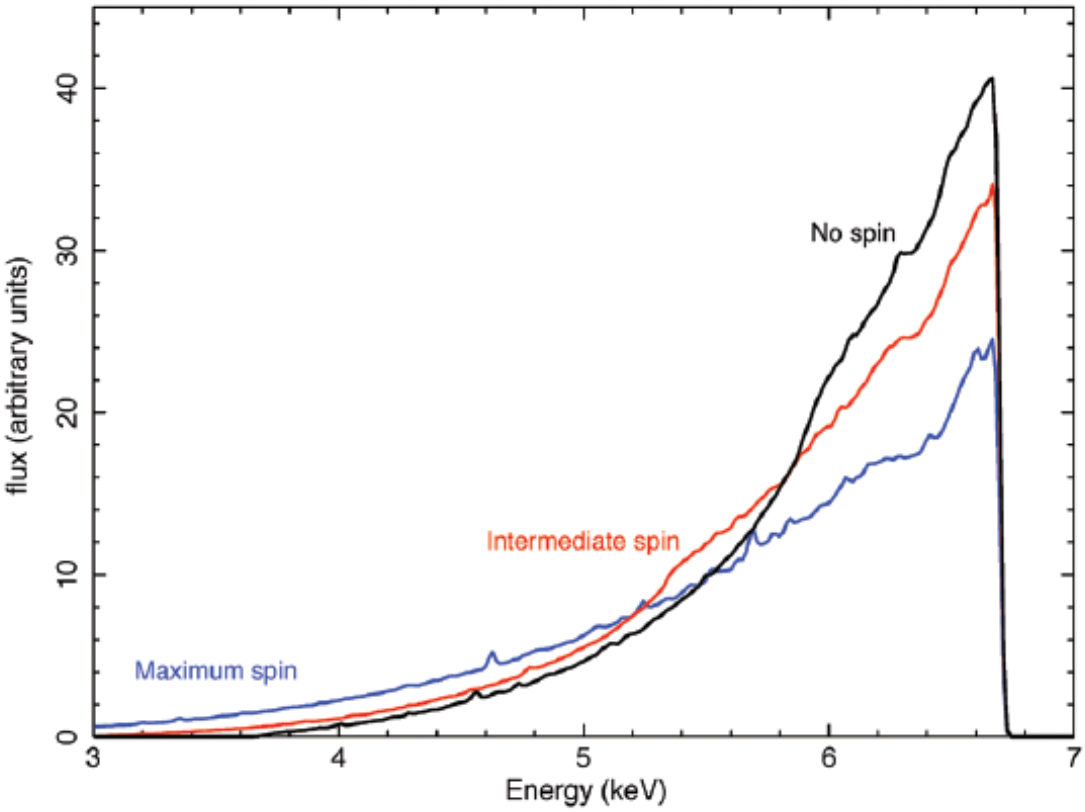

Figure 1.10: The effect of black hole spin on the broadened iron line. Increased spin allows for a smaller ISCO resulting in more disc material experiencing the extreme effects of being so close to the black hole. Figure from Gallo (2011).

1.4.2 Line Models

Studying the emission lines in AGN spectra is effectively done through the use of modelling techniques designed for the spectral fitting package XSPEC (Arnaud 1996). One of the first models produced to study such features is DISKLINE (Fabian et al. 1989) which models a single emission line produced by a relativistic accretion disc around a Schwarzschild ($a = 0$) black hole. To properly model a full spectrum the same blurring effect applied to the single emission line in DISKLINE must also be applied to all emission lines, as they originate from the same material in the accretion disc. RDBLUR was designed as a blurring kernel to relativistically blur the emission from the accretion disc. Laor (1991) then proceeded to create a Kerr ($a = 0.998$) black hole emission line model, LAOR, which has a corresponding blurring kernel KDBLUR in order to study emission lines from the accretion disc surrounding a maximally spinning black hole.

1.5 Emissivity Profiles

As discussed briefly in an earlier section, the exact geometry of the corona remains a mystery. The structure of the X-ray source, however, may be probed by studying the illumination pattern of the accretion disc by the corona (emissivity profile). Throughout this work the illumination profile (photons incident on the disc) and emissivity profile (photons processed and re-emitted by the disc) are treated as equivalent, and thus the terms used interchangeably. Laor (1991) defined the emissivity, $\epsilon(r)$, as the reflected flux from the accretion disc as a function of radius measured in the frame of the accretion disc. The reflection spectrum

observed at infinity, $F_0(\nu_0)$, is therefore of the form:

$$F_0(\nu_0) = \int \epsilon(r_e) I_r \left(\frac{\nu_e}{g}\right) T(r_e, g)\, dg r_e dr_e \tag{1.1}$$

where I_r is the rest-frame reflection from the disc, $T(r_e, g)$ is the transfer function which projects the rays to the observer, and is integrated over all redshift values $g = E_{\rm obs}/E_{\rm em}$, where $E_{\rm obs}$ is the energy measured by an observer and $E_{\rm em}$ is the energy emitted, over all radii r of the accretion disc such that the emitted line is shifted to ν_0. The emissivity profile can be measured from AGN data and fit with a power law in order to gain insight into the nature of the X-ray source (e.g. Wilkins & Fabian 2011). Simulating various corona geometries and exploring the emissivity profiles produced allows for comparisons to be made between theoretical models and the measured profiles obtained from AGN data.

1.5.1 Lamppost Model

There is evidence to suggest that the corona geometry may be either a compact or extended atmosphere-like source, both at some height above the accretion disc. For modelling purposes it is often considered a point-like source hovering over the black hole spin axis (i.e. the "lamppost" model). This is not an unreasonable simplification since current spectral (e.g. Brenneman & Reynolds 2006; Gallo et al. 2013; Parker et al. 2015) and timing studies (e.g. Fabian et al. 2009, 2013; Zoghbi et al. 2010) do support a compact and centrally located corona. The isotropic emission from this point source corona will illuminate the accretion disc, with the flux of X-rays from the corona decreasing as radius r along the accretion disc

increases. Classically, we know that the incident flux from the corona on the accretion disc, the emissivity, will be proportional to r^{-3} at large radii. For small r, however, the emissivity will increase dramatically as light bending effects focus light rays on the inner regions of the accretion disc. Therefore, the emissivity profile for point sources is expected to fall off steeply for small r before following a r^{-3} profile for large r (e.g. Miniutti et al. 2003).

1.5.2 Other Geometries

Though the lamppost model may be an adequate approximation for some objects, in a growing number of cases it is insufficient (e.g. WF12, Wilkins & Gallo 2015b). Modelling the emissivity profiles produced by more extended geometries such as ring-like structures (e.g. Suebsuwong et al. 2006), and extended slabs (which may be seen as representing the bulk of a more detailed extended model) (e.g. WF12) has been shown to accurately reproduce measured profiles from AGN data. WF12 were able to successfully show through comparing simulated emissivity profiles with observational data that the extended nature of the corona can be detected in the emissivity profile of the blurred reflection spectrum. Collimated sources (e.g. Dauser et al. 2013) provide another plausible corona geometry, more fitting in cases where beaming of the X-ray source is evidenced.

1.5.3 Variability

Point source and extended corona geometries can both provide good fits to AGN data, though until now we have assumed an unchanging geometry with time. Recent work points towards a dynamic nature of the corona suggesting that the geometry itself undergoes dra-

matic changes based on the X-ray flux emitted by the source (e.g. Wilkins et al. 2014; Wilkins & Gallo 2015a). For the narrow line Seyfert 1 (NLS1) galaxy 1H 0707–495 the emissivity profile was consistent with a twice-broken power law. The profile was steep in the inner region where light bending is dominant, flat at intermediate radii where the corona blankets the disc, and drops with r^{-3} at large distances. Further analysis shows the emissivity profile, and hence the geometry of the corona, may change depending on the flux of the source. For example, Wilkins et al. (2014) found the corona in 1H 0707–495 to be extended in the bright state but compact when the source was dim, showing a dynamic nature of the corona undergoing phase changes and altering its geometry significantly during these processes. Wilkins & Gallo (2015a) found for NLS1 galaxy Markarian 335 that during high flux periods the corona was large and extended while in low flux periods the source was much more compact.

The emissivity profile is a strong probe for geometry of the corona that can be used alongside various other tools including the reflection fraction (e.g. Wilkins 2015; Wilkins & Gallo 2015b) and time-lag analysis (e.g. Wilkins & Fabian 2013) in order to gain further insights into the nature of the X-ray source.

Chapter 2

Ray Tracing & Calculations

The theoretical emissivity profiles shown throughout this paper were produced via general relativistic ray tracing simulations of various corona geometries above a rotating Kerr black hole. The Kerr metric in Boyer-Lindquist co-ordinates follows as:

$$\begin{aligned} ds^2 = c^2 \left(1 - \frac{2\mu r}{\rho^2}\right) dt^2 + \frac{4\mu a c r \sin^2\theta}{\rho^2} dt d\varphi - \frac{\rho^2}{\Delta} dr^2 - \rho^2 d\theta^2 \\ - \left(r^2 + a^2 + \frac{2\mu a^2 r \sin^2\theta}{\rho^2}\right) \sin^2\theta d\varphi^2 \end{aligned} \tag{2.1}$$

where $a \equiv J/Mc$ is the Kerr parameter[1], $\mu \equiv GM/c^2$, $\rho^2 \equiv r^2 + a^2\cos^2\theta$, and $\Delta \equiv r^2 - 2\mu r + a^2$. Making use of the convention $c = \mu = 1$ provides units of gravitational radii such that $r_g = GM/c^2$.

The exact method in which the ray tracing simulations were performed, along with the construction of the X-ray source, is presented in WF12 and is summarized briefly here.

[1]The Kerr parameter is related to the dimensionless spin parameter as $a_\star = a/r_g$.

Photons are propagated along null geodesics in the spacetime surrounding a Kerr black hole until they reach the accretion disc, the event horizon, or escape the system. The X-ray source is constructed based on the geometry to be studied (e.g. a point source, cylindrical, spheroidal, ellipsoidal, or conical geometry) with rays starting a random locations within the defined source region. A tetrad of basis vectors, with one time-like ($\mathbf{e}'_{(t)}$) and three space-like ($\mathbf{e}'_{(1)}$, $\mathbf{e}'_{(2)}$, $\mathbf{e}'_{(3)}$) vectors, is constructed for each source type (e.g. stationary, rotating, or beamed) ensuring that they satisfy:

$$\mathbf{e}'_{(\alpha)} \cdot \mathbf{e}'_{(\beta)} = g_{\mu\nu} e^{\mu}_{(\alpha)} e^{\nu}_{(\beta)} = \eta_{(\alpha)(\beta)} \tag{2.2}$$

where $g_{\mu\nu}$ is the metric tensor corresponding to the Kerr metric in Equation 2.1 and $\eta_{(\alpha)(\beta)}$ is the Minkowski metric.

Once the rays have been initiated within the source region and propagated to the accretion disc (those that reach the event horizon or escape the system are disregarded) they are summed in radial bins for annuli of area $A\,(r, dr)$ on the disc, giving the number of photons as $N\,(r, dr)$. Accounting for redshift effects on photon energy dividing by a factor of g^2 gives the emissivity profile as:

$$\epsilon\,(r) = \frac{N\,(r, dr)}{g^2 A(r, dr)} \tag{2.3}$$

where $g = E_{\rm em}/E_{\rm obs}$ with $E_{\rm em}$ being the energy emitted and $E_{\rm obs}$ being the energy measured by an observer. By calculating the emissivity profiles of various corona geometries and

analysing the differences between them raises the possibility of detecting different source geometries in AGN data.

Chapter 3

Point Sources

The venture into examining different corona geometries begins with the simple stationary, isotropic point source (the aforementioned "lamppost" model). In the simulations, the source is held at a fixed height z on the spin axis above the accretion disc of a rotating Kerr black hole with dimensionless spin parameter $a = 0.998$, as shown in Figure 3.1.

As in WF12 a set of basis vectors must be constructed for this source model in order to evaluate the energies of the emitted photons as well as the angle of photon emission according to the rest frame of an observer outside of the source frame of the corona. In this framework, the space-like basis vectors are such that they form a Cartesian coordinate system in the observer's frame. The source may also be given a rotational velocity $\Omega = d\varphi/dt = \left(a \pm x^{3/2}\right)^{-1}$ about the spin axis, where x is the distance from the spin axis. For a stationary, isotropic point source $\Omega = 0$. Constructing the tetrad of basis vectors, using the method in Appendix A of WF12, for a point source yields:

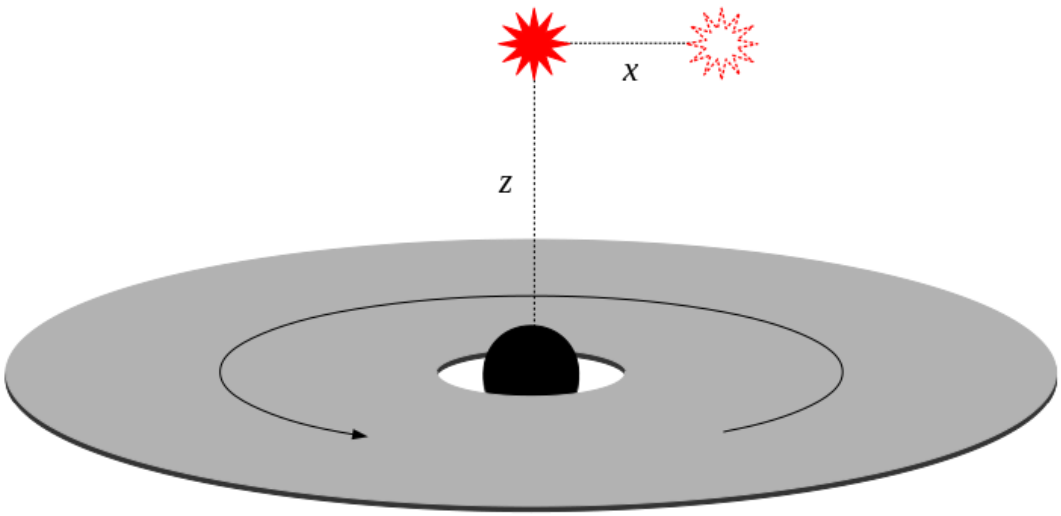

Figure 3.1: A schematic representation of a stationary, isotropic point source located at a height z with displacement x from the spin axis above a rotating Kerr black hole and accretion disc.

$$
\begin{aligned}
\mathbf{e}'_{(t)} &= \sqrt{\frac{1}{g_{tt} + 2\Omega g_{\varphi t} + \Omega^2 g_{\varphi\varphi}}}\,(1, 0, 0, \Omega) \\
\mathbf{e}'_{(1)} &= \left(0, \sqrt{\frac{-1}{g_{rr}}}, 0, 0\right) \\
\mathbf{e}'_{(2)} &= \left(0, 0, \sqrt{\frac{-1}{g_{\theta\theta}}}, 0\right) \\
\mathbf{e}'_{(3)} &= \sqrt{\frac{1}{g_{tt} + 2\Omega g_{\varphi t} + \Omega^2 g_{\varphi\varphi}}}\,(g_{\varphi t} + \Omega g_{\varphi\varphi}, 0, 0, \Omega g_{\varphi t} - g_{tt})
\end{aligned}
\tag{3.1}
$$

Ray tracing simulations were run for stationary, isotropic point sources at $z = 1.5r_g$, $z = 5r_g$, $z = 10r_g$, and $z = 20r_g$. The results of these simulations are shown in Figure 3.2. The general shape of all lines on the plot resembles a twice-broken power law with a steeply

falling inner profile and an outer profile following r^{-3}. The steep slope of the inner profile is a result of time dilation greatly enhancing the flux of photons incident on the innermost region of the accretion disc according to observers closest to the black hole. The profile shape for point sources obtained here as well as the trend with increased height agree with similar works studying the lamppost geometry (e.g. Miniutti et al. 2003; Suebsuwong et al. 2006;WF12;Dauser et al. 2013; Dovciak et al. 2014).

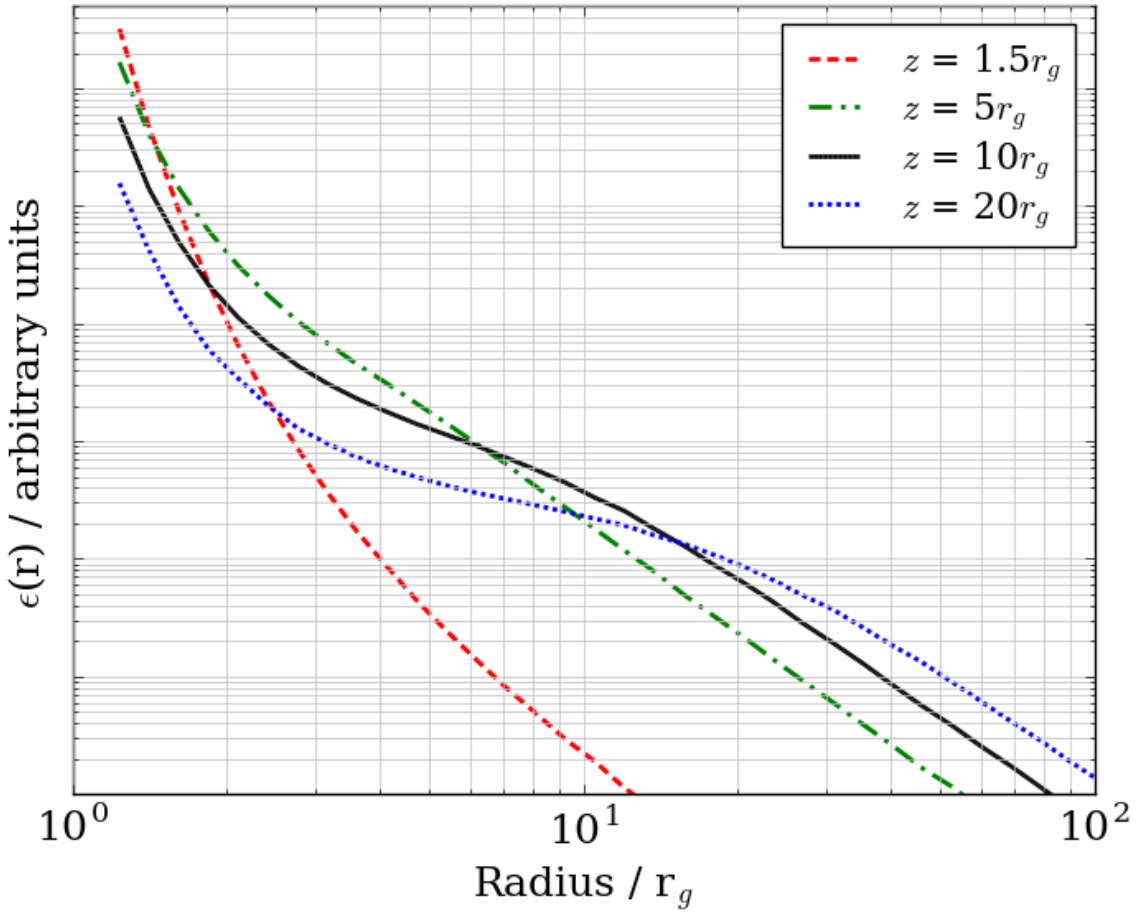

Figure 3.2: A comparison of point sources at four different heights ranging from $z = 1.5r_g$ to $z = 20r_g$ located on the rotation axis of a black hole with $a = 0.998$.

Trials with spin parameter $a < 0.998$ act to increase the innermost stable circular orbit

(ISCO) and therefore truncate the profile at small r. The spin parameter is held at $a = 0.998$ for all following work.

The first property of the point source model is the height of the corona above the black hole. Figure 3.2 shows how the height of the source effects its emissivity profile. For a point source at $z = 1.5r_g$ the effects of general relativity are extreme. Most of the photons landing on the accretion disc are focused tightly around the black hole and immediate vicinity. Increasing the height of the source produces a twice-broken power law shape in the emissivity profile that becomes pronounced for larger values of z, as found in WF12.

For $r \approx z$ in the latter three cases a turnover exists in the profile at the second break point. This second break-point in the twice-broken power law description is measured directly from the Fe Kα line in the reflection spectrum of AGN and can be constrained to within $\sim$15–30 per cent error (e.g. Wilkins & Fabian 2011; Wilkins & Gallo 2015a). Common to all cases is the outer profile which follows r^{-3} as in the case of the classical description of a point source above an infinite plane.

The second property of the point source geometry is displacement from the spin axis, given by x, the results of which are shown in Figure 3.3 for a point source located at $z = 10r_g$. As the source moves away from the spin axis the inner disc receives fewer photons while the outer disc receives proportionally more. Particularly, where $r \approx x$ the break in the emissivity profile is accentuated indicating that (other than the inner disc) the largest number of photons land on the disc directly under the point source. If these sources were each to be co-rotating with the accretion disc, a more pronounced break would be visible in the profile as rays are beamed in the direction of motion, focusing the emission and further

increasing the number of photons received by the disc at $r \approx x$, as shown in WF12. The axisymmetric nature of the Kerr spacetime means that this example of a displaced point source is equivalent in disc illumination to a ring-like source geometry as we consider the emissivity profiles as a function of r only and are therefore azimuthally averaged.

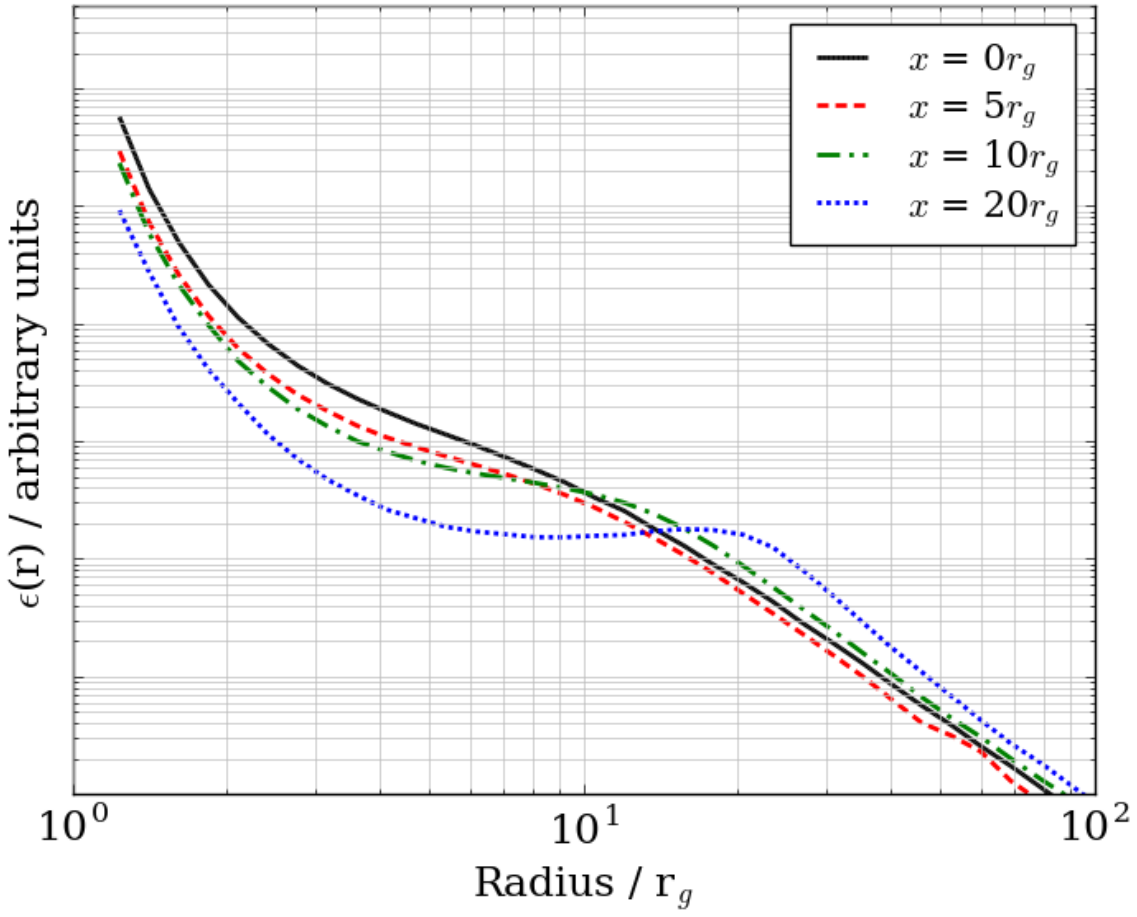

Figure 3.3: Point source coronae at $z = 10r_g$ with displacements $x = 0r_g$ to $x = 20r_g$ away from the rotation axis.

Thus far, we have been assuming the value of Γ, the photon index, of the power law spectrum emitted from the corona incident on the accretion disc as $\Gamma = 2.0$. We may vary this value and study its effect on the emissivity profile of a point source, shown in Figure 3.4.

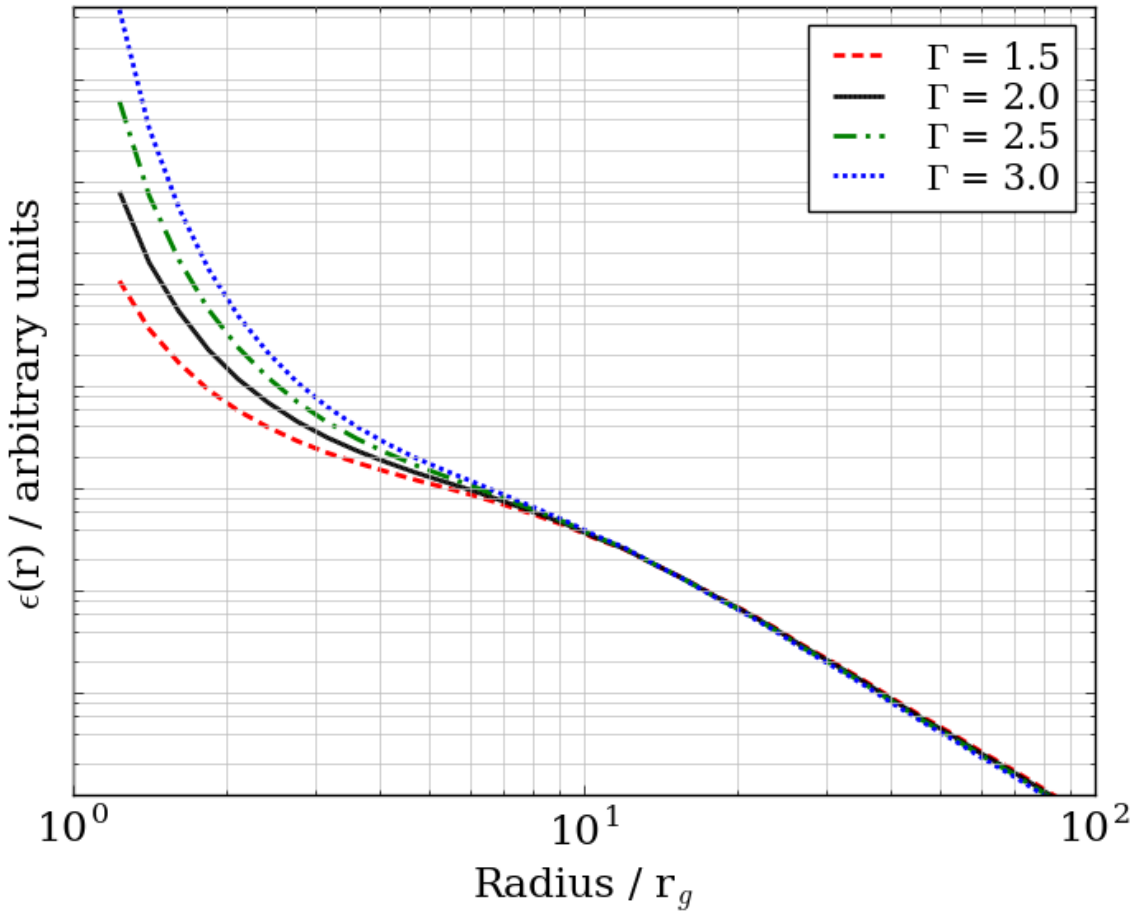

Figure 3.4: Emissivity profiles produced by point sources at height $z = 10r_g$ with varying values of photon index Γ for the incident spectrum.

The variation of the photon index requires a variant of Equation 2.3 where g^2 in the denominator is replaced by g^Γ. This arises as the number of photons travelling along any given ray must be conserved for different Γ, requiring the energy correction, previously g^2, to be adjusted accordingly, to g^Γ, in order to properly account for the change in the number of photons in each bin of the emissivity profile. As can be seen in the plot, by using a spectrum with a steeper continuum we have increased the slope of the profile for the innermost region of the accretion disc. Beyond $r \approx 10r_g$, however, the effect of changing the value of Γ quickly

becomes minimal. This effect, though important, will not be further studied in the cases to come as the result is well illustrated with this single example. With this preliminary analysis of point sources complete it is now possible to examine more physically plausible examples of extended corona geometries.

Chapter 4

Extended Sources

Extended source geometries can be simulated as a sum of point sources within a defined region, producing an optically thin extended corona geometry. Each of the rays within the constructed geometry is given a random initial position and random direction with distribution such that each point emits isotropically in its own rest frame. Photons are then propagated along null geodesics, as in Section 3, until they either reach the disc, are lost beyond the event horizon, or escape the system. Note that, as in WF12, extended sources are assumed to have a homogeneous emissivity profile. This means that finding the best-fitting profile to an observed spectrum finds the geometry that is responsible for the bulk of the coronal emission.

4.1 Cylindrical

We begin the extended source geometry analysis with a rotating cylindrical slab at height z above the accretion disc. The cylinder has thickness Δz and radial extent $R_{\rm cor}$, as seen in Figure 4.1. In this geometry points are assumed to co-rotate with the portion of the disc directly beneath, if, for instance, they are accelerated by field lines anchored to the disc beneath (e.g. WF12). This gives points in the corona a rotational velocity of $\Omega = d\varphi/dt = \left(a \pm x^{3/2}\right)^{-1}$ where x is the distance from the spin axis.

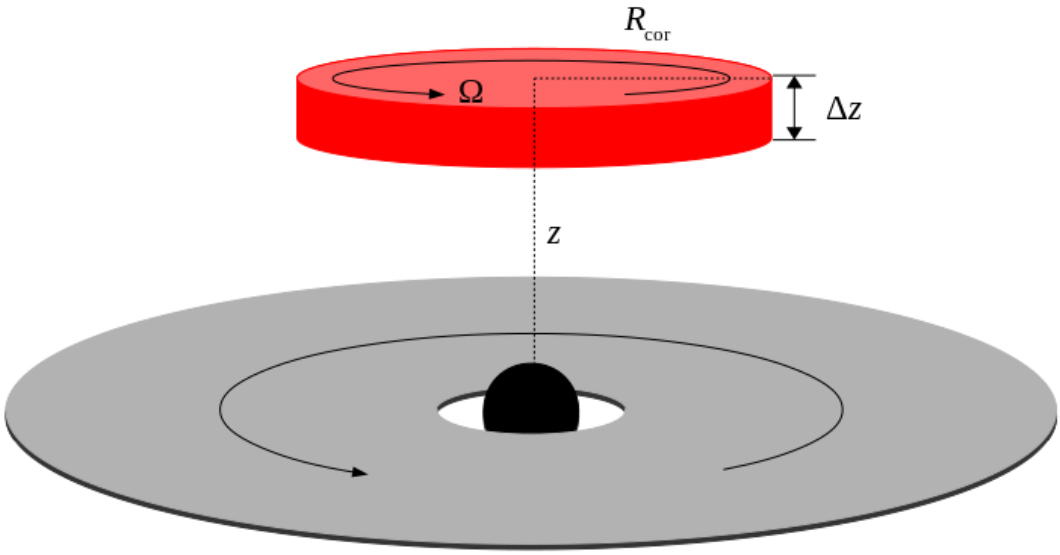

Figure 4.1: A cylindrical slab corona geometry rotating with $\Omega = d\varphi/dt$ located at a height z above a rotating Kerr black hole. It has thickness Δz and extends radially a distance $R_{\rm cor}$ over the accretion disc.

In Figure 4.2 we compare the emissivity profile produced by a cylindrical slab, centred on $z = 10r_g$ with radial extent $R_{\rm cor} = 10r_g$ and thickness $\Delta z = 2r_g$, to a point source at

$z = 10r_g$. It can be seen that in the case of the slab corona the photons landing on the accretion disc are spread over the outer radii of the disc causing the profile to be flattened in comparison with that of the point source. This result is to be expected from the extended nature of the slab geometry as we are essentially summing the emissivity profiles of all point sources contained within the region defined by the cylindrical source.

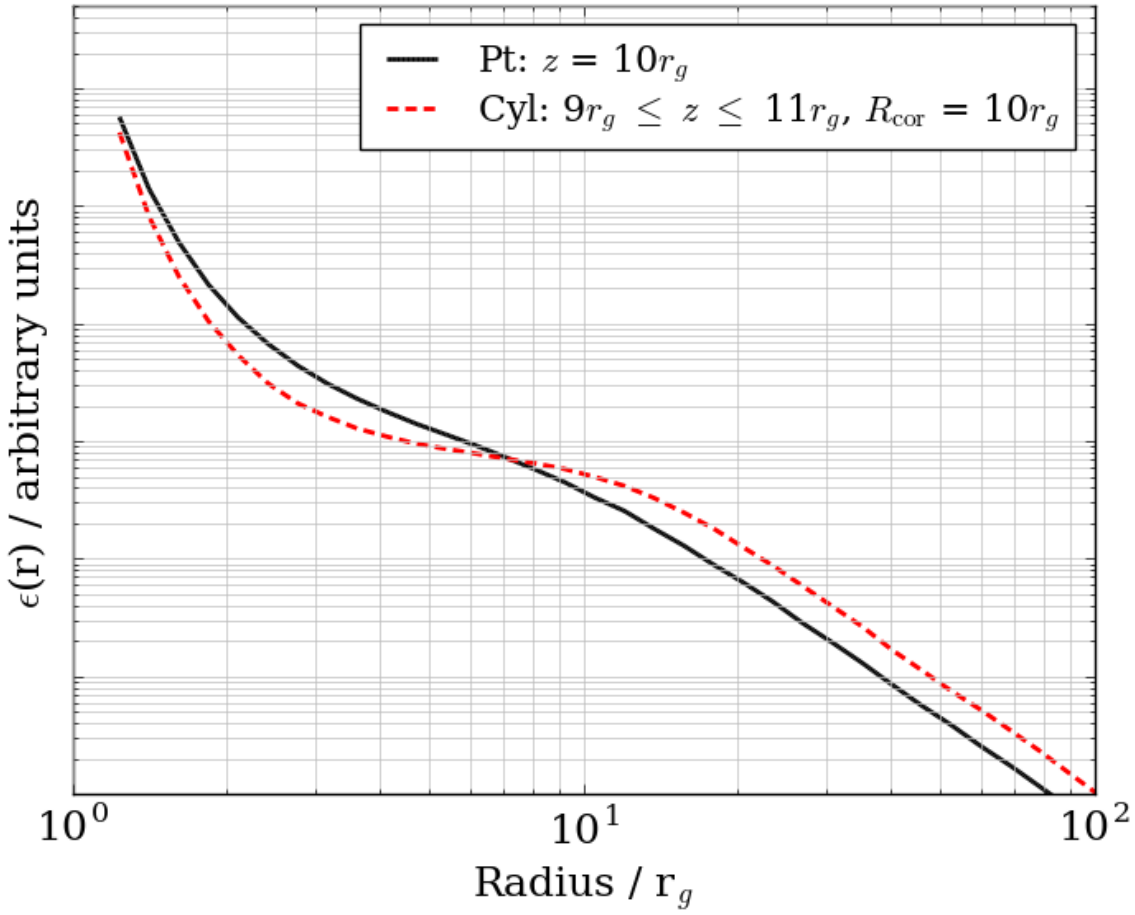

Figure 4.2: A comparison of a point source at $z = 10r_g$ with an extended cylindrical slab centred on $z = 10r_g$ with extent $R_{\rm cor} = 10r_g$ and thickness $\Delta z = 2r_g$.

At just over $r = 10r_g$ a break point in the profile of the disc is produced in the case of the cylindrical corona, corresponding with the outer edge of the slab. The profile then falls

off with slope approximately equal to that of the outer profile produced by point source at large radii. The twice-broken power law shape is prevalent in both cases, though the flattened midsection of the emissivity profile resulting from the slab geometry enhances the shape.

By simulating different source heights above the accretion disc for extended cylindrical models, the emissivity profiles in Figure 4.3 are produced. Placing the corona closer to the accretion disc results in more of the emission being focused on the inner region of the disc, as seen by the enhanced inner profile for the lowest sources. By moving the slab further away from the disc, to be centred at $z = 10r_g$, the inner region of the accretion disc receives a smaller fraction of the emitted photons. Also included is a thick slab of $\Delta z = 7r_g$ that encapsulates the two other slabs centred on $z = 5r_g$ and $z = 10r_g$. From this we can see that thickness of the corona does not significantly impact the shape of the emissivity profile, retaining its twice-broken shape. Overall, increasing distance from the accretion disc acts to stretch the shape of the profile and thus distribute photons more evenly across the disc.

Extending the cylindrical geometries radially produces the emissivity profiles in Figure 4.4. By reducing the radial extent of the slab the break in the profile moves to a smaller radius, and conversely increasing the extent moves the break point out to larger radii. As noted previously, the break point in the emissivity profile traces the outer edge of the slab which allows us to measure the radial extent of the source, as shown in WF12.

Comparing the results in Figures 4.3 and 4.4 shows that, in the cases studied, the extent of the slab produces a larger effect on the emissivity profile than does the height of the source. This indicates that for extended geometries covering a large portion of the

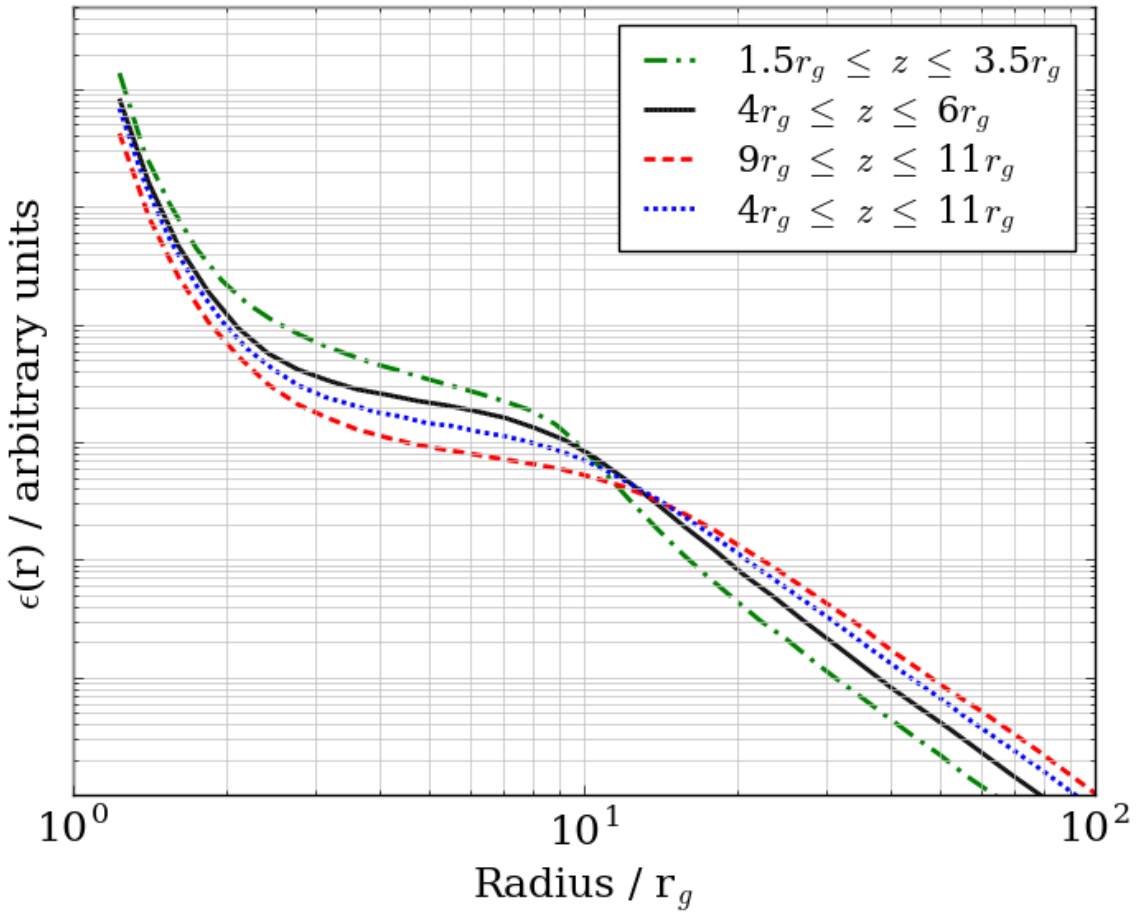

Figure 4.3: The effect of height on emissivity profiles of cylindrical sources centred on $z = 2.5r_g$, $z = 5r_g$, and $z = 10r_g$ with $R_{\rm cor} = 10r_g$ and of thickness $\Delta z = 2r_g$, with a thick slab centred on $z = 7.5r_g$ of thickness $\Delta z = 7r_g$.

disc radial extent is more easily determined than source height and has a more significant impact on the emissivity profile overall, as found in WF12. With an understanding of how changes in location and size of an extended source geometry affect the emissivity profile it is now possible to examine different configurations, such as a hemisphere placed directly on the accretion disc.

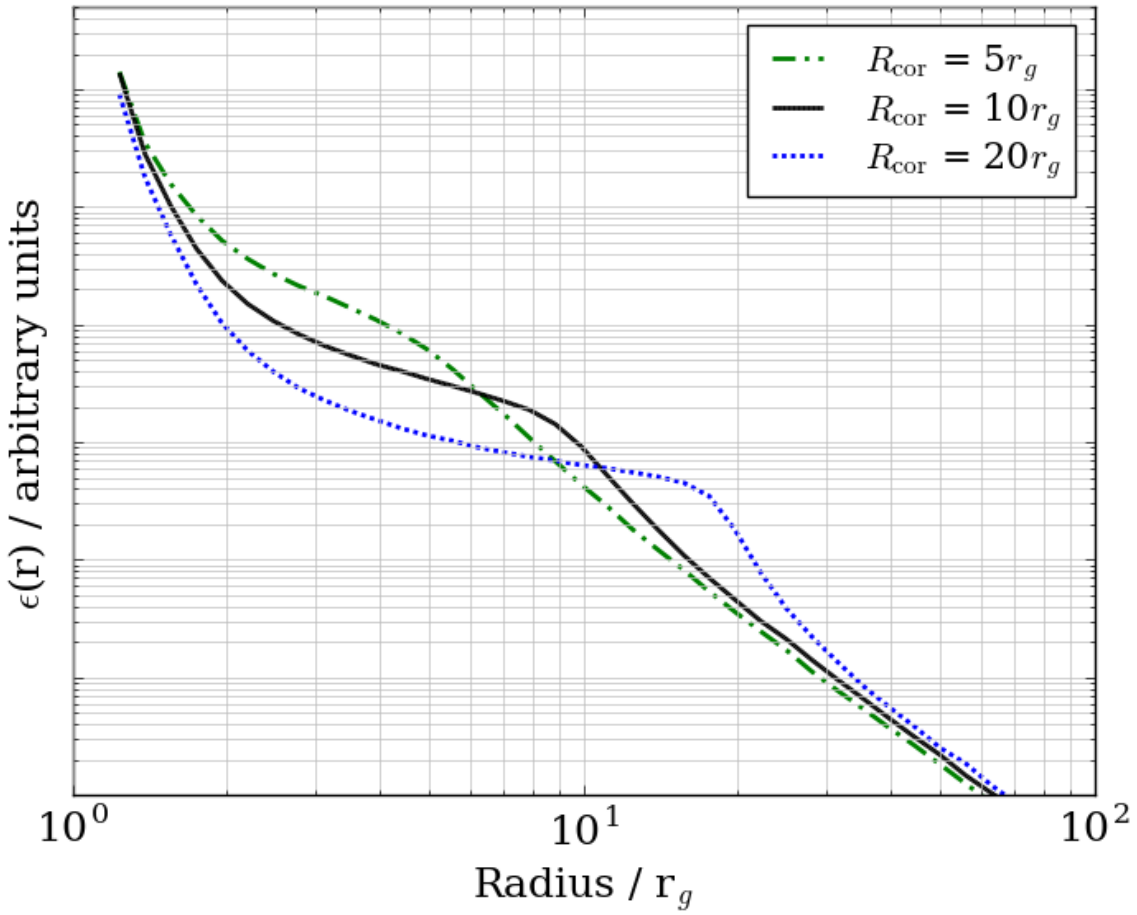

Figure 4.4: Various cylindrical sources with radial extents $R_{\mathrm{cor}} = 5r_g$, $R_{\mathrm{cor}} = 10r_g$, and $R_{\mathrm{cor}} = 20r_g$ all centred on $z = 2.5r_g$ and of thickness $\Delta z = 2r_g$.

4.2 Spheroidal

For the point source and cylindrical slab, the source was located at some height z above the black hole and accretion disc system. In this case a hemisphere of radius R_{sph} rotating with $\Omega = d\varphi/dt$, as defined in Section 3, is placed on the accretion disc, encapsulating the black hole itself, as shown in Figure 4.5.

Referring back to Figure 4.3 and the observed effect of moving an extended source closer

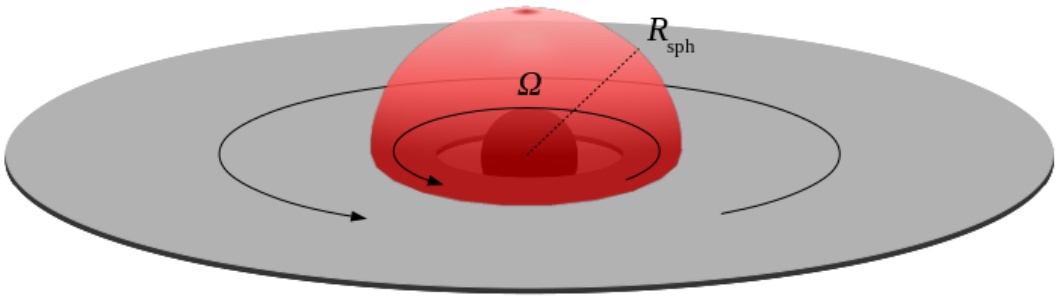

Figure 4.5: A spheroidal corona geometry rotating with $\Omega = d\varphi/dt$ and radius R_{sph} located on the accretion disc of a rotating Kerr black hole.

to the black hole, we already have an intuition that the emissivity profile will exhibit a shortened flatter mid-section as we are close to the black hole.

Figure 4.6 compares the emissivity profiles produced by two sets of like-sized spheroidal and cylindrical extended geometries placed on the accretion disc. The profiles produced are of similar shape dropping from their flattened midsection at the same radius for like sized sources. Spherical geometries produce a more pronounced break and a decreased number of photons reaching the outer regions of the accretion disc. This result is not unexpected as the spheroidal sources are smaller in volume than similarly sized cylindrical slabs by a factor of one-third, with the missing volume being most significant at the outer edge of the source. As such, the spheroidal geometries emit fewer photons at the maximum radial extents than the cylindrical sources, producing the discussed results in the profiles.

Moving forward, it is not unreasonable to argue that a spheroidal corona may become oblate due to the orbital motion of the corona. Moreover, if the corona is in fact formed by the magnetic fields anchored on the accretion disc, their movement and rotation would also

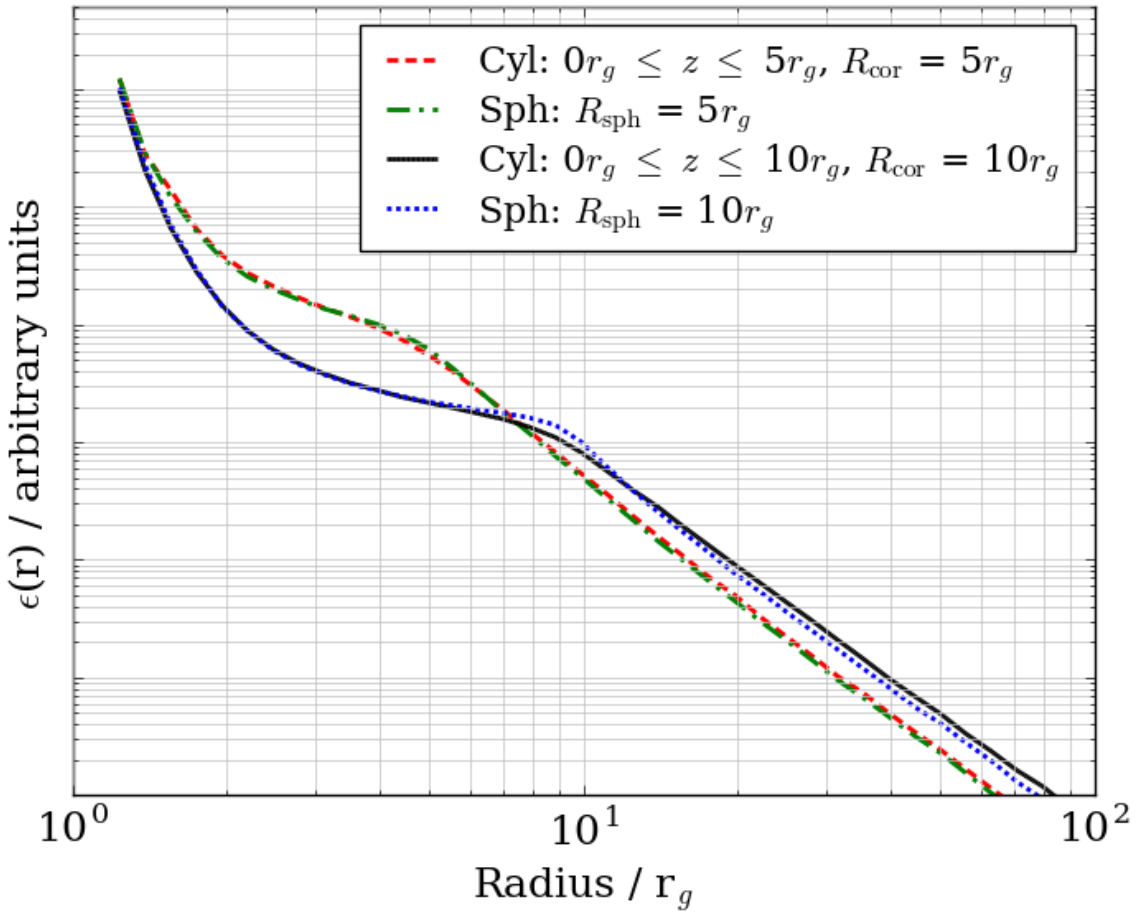

Figure 4.6: Comparing two sets of cylindrical and spheroidal corona geometries of similar size located on the accretion disc.

produce an oblate deformation of the spheroid. Therefore, it is plausible that a spheroidal geometry would warp into an ellipsoidal configuration, with semi-major axis a and semi-minor axis b as in Figure 4.7.

Comparisons of the emissivity profiles of similarly sized spheroidal and ellipsoidal coronae can be seen in Figure 4.8. By decreasing the height b of the spheroidal geometry to become more ellipsoidal, a decreased number of photons reach the outer extent of the accretion disc while an increased number are observed to land on the inner region of the disc. This change

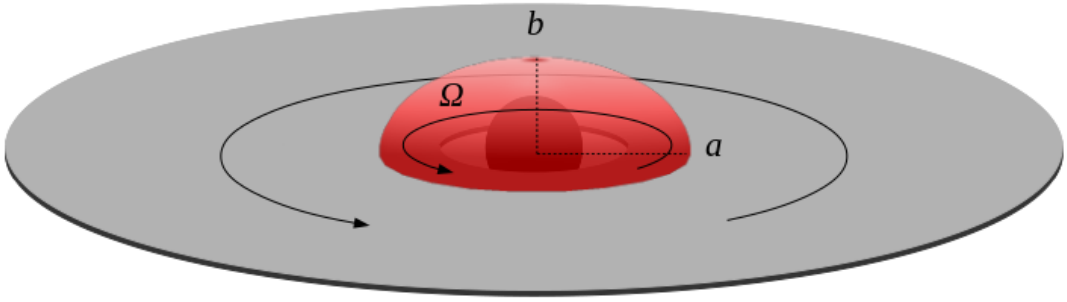

Figure 4.7: An ellipsoid corona geometry rotating with $\Omega = d\varphi/dt$ with semi-major axis a and semi-minor axis b located on the accretion disc of a rotating Kerr black hole.

produces a more pronounced break point for reductions in the value of b. These results are expected as decreasing the height of the spheroidal shape removes a portion of the source located furthest away from the black hole, reducing the number of photons reaching the outer disc. This effect is that fewer photons are able to reach the outer portion of the disc and are emitted closer to the black hole, being drawn into the region of the inner few radii of the accretion disc.

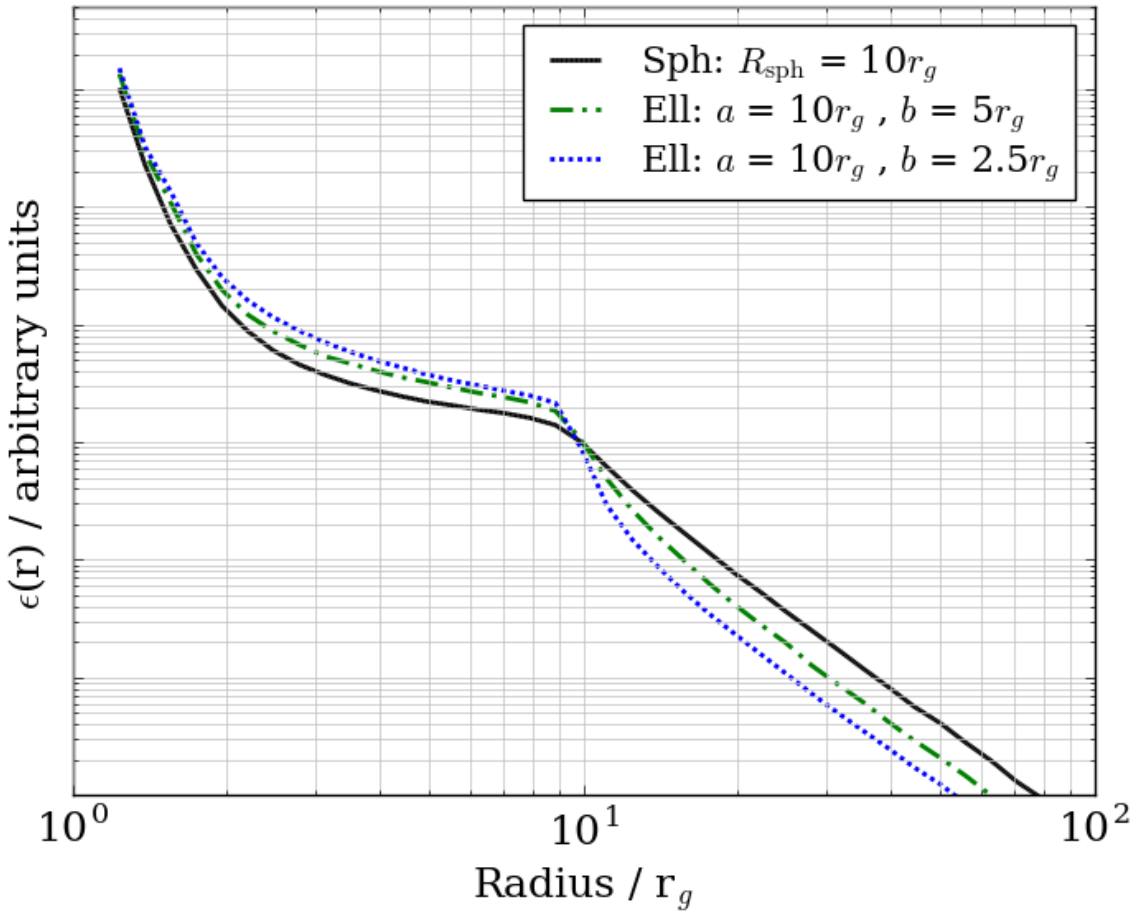

Figure 4.8: Investigating the effect of height on spheroidal corona geometries located on the accretion disc with semi-major axes $a = 10r_g$ and varying semi-minor axes $b = 2.5r_g$, $b = 5r_g$, and $b = 10r_g$.

4.3 Conical

In all of the extended geometries studied thus far we have been examining emissivity profiles produced by predominantly radially extended sources. With such corona geometries studied both on the disc and at some height z above it we may move to another physically motivated source configuration with a focus on being vertically extended to simulate the base of a jet.

Conical geometries opening away from the black hole pose an attractive and physically

motivated source geometry as in the base of a jet in AGN (Blandford & Znajek 1977; Falcke & Biermann 1995; Ghisellini et al. 2004). The simulation of conical sources can be done utilizing the same basis vectors previously derived for a source rotating with $\Omega = d\varphi/dt$ and by constraining a sum of point sources within a region defined with height z and opening angle ψ (Figure 4.9).

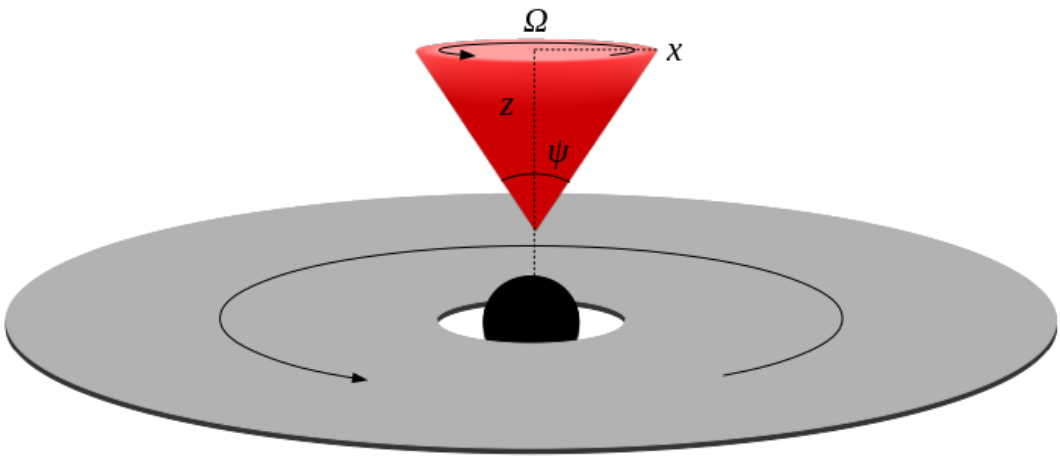

Figure 4.9: A schematic of the conical corona geometry rotating with $\Omega = d\varphi/dt$ at height z above a rotating Kerr black hole and with opening angle ψ that extends a distance x over the accretion disc.

Neither the cylindrical slab nor spheroidal geometries provide an appropriate comparison to the conical source as they are both much larger in volume. Conical sources with small opening angles ψ are more plausible candidates for jet-like source bases as too great of an angle would produce a much weaker focusing of the rays in the direction of opening. Therefore, point sources will be used as the basis for comparison throughout this section.

In Figure 4.10 two conical geometries of height $1.5r_g \leq z \leq 5r_g$ and $5r_g \leq z \leq 10r_g$ with

opening angle $\psi = 10^{\circ}$ are compared to two point sources at heights $z = 5r_g$ and $z = 10r_g$. The comparison of the emissivity profiles show that in both cases the point source located at the top of the respective cone produces a profile shape exceptionally similar to that of the matching conical source. This result is not entirely unexpected as the opening angle of the conical sources must remain small and therefore the majority of the source volume is located closer to the top of the cone than the vertex. Similar findings were obtained by Dauser et al. (2013) comparing point sources to vertically extended coronae, where it was determined that a point source at some intermediate location between the base and top of a conically shaped geometry could produce a very similar emissivity profile.

This result does prompt the need to further test the difference between point sources and conical geometries in different ways. We define the reflection fraction, R, as:

$$R = \frac{N_{\text{disc}}}{N_{\text{escaped}}} \tag{4.1}$$

where N_{disc} is the number of photons that land on the accretion disc, producing an observed reflection spectrum, and N_{escaped} is the number of photons that escape the system entirely, forming the observed power law continuum.

Observationally, we cannot measure the number of photons incident on the accretion disc due to various processes that take place once the photon reaches the disc that result in a different number of reflected photons. Assuming that the coronal emission is constant over time, however, allows for the accretion disc to eventually reach an equilibrium state such that the energy incident on the disc from the corona is equal to the energy output by

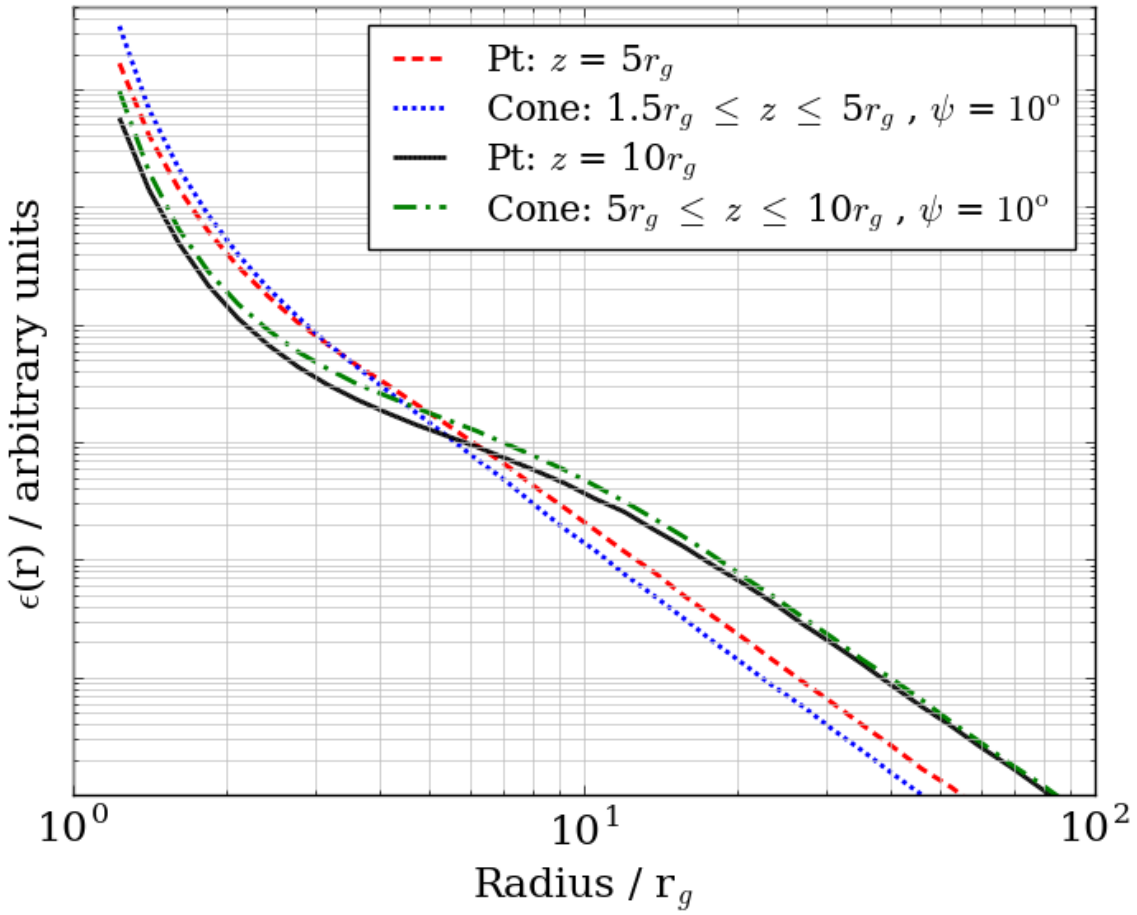

Figure 4.10: Conical corona geometries compared with point sources placed at the maximum height of the displayed cones with opening angles $\psi = 10°$ located a distance z above the black hole.

the disc. Thus an approximation to the fraction of photons that are incident on the disc can be obtained from a reflection fraction defined as the ratio of reflected to continuum flux.

Using Equation 4.1 it is found that for the conical source with height $5r_g \leq z \leq 10r_g$ (Figure 4.10) $R = 1.775$ and for the point source at $z = 10r_g$ that $R = 1.487$. Furthermore, for the cone at $1.5 \leq z \leq 5r_g$ $R = 3.246$ and for the point source at $z = 5r_g$ that $R = 2.114$. The reflection fraction of conical geometries are not significantly different from point sources

if they are sufficiently far away from the black hole. In the case of the sources within $5r_g$ of the black hole, the extended nature of the source down to $z = 1.5r_g$ does come into effect as more photons here are focused back down onto the innermost regions of the accretion disc whereas in the case of the point source all of the photons emitted are at $z = 5r_g$ with a much reduced effect of gravity from the singularity.

As in the previous sections we may begin the further analysis of conical sources by varying the height above the accretion disc and black hole, as seen in Figure 4.11. The results produced here are consistent with expectations: a source closer to the black hole exhibits a nearly featureless profile with less photons landing on the outer disc while a source further away from the black hole accentuates the underlying twice-broken nature of the profile with a flattened midsection.

Further exploration naturally leads to the variance of the opening angle of the cone, which has the effect of increasing the radial extent over the accretion disc. The results shown in Figure 4.12 were produced by a cone at $5r_g \leq z \leq 10r_g$ and indicate that by decreasing the opening angle the photons become further focused on the innermost radii of the accretion disc while increasing the value of ψ allows for more photons to land at larger radii. In fact, the conical source with the smallest angle produced an emissivity profile more similar to a point source while the profile produced by the cone with a larger opening angle resembles an extended profile such as those seen in the slab cases. Between the three examples shown in Figure 4.12 the profile shape differs far less in comparison to the effect of height.

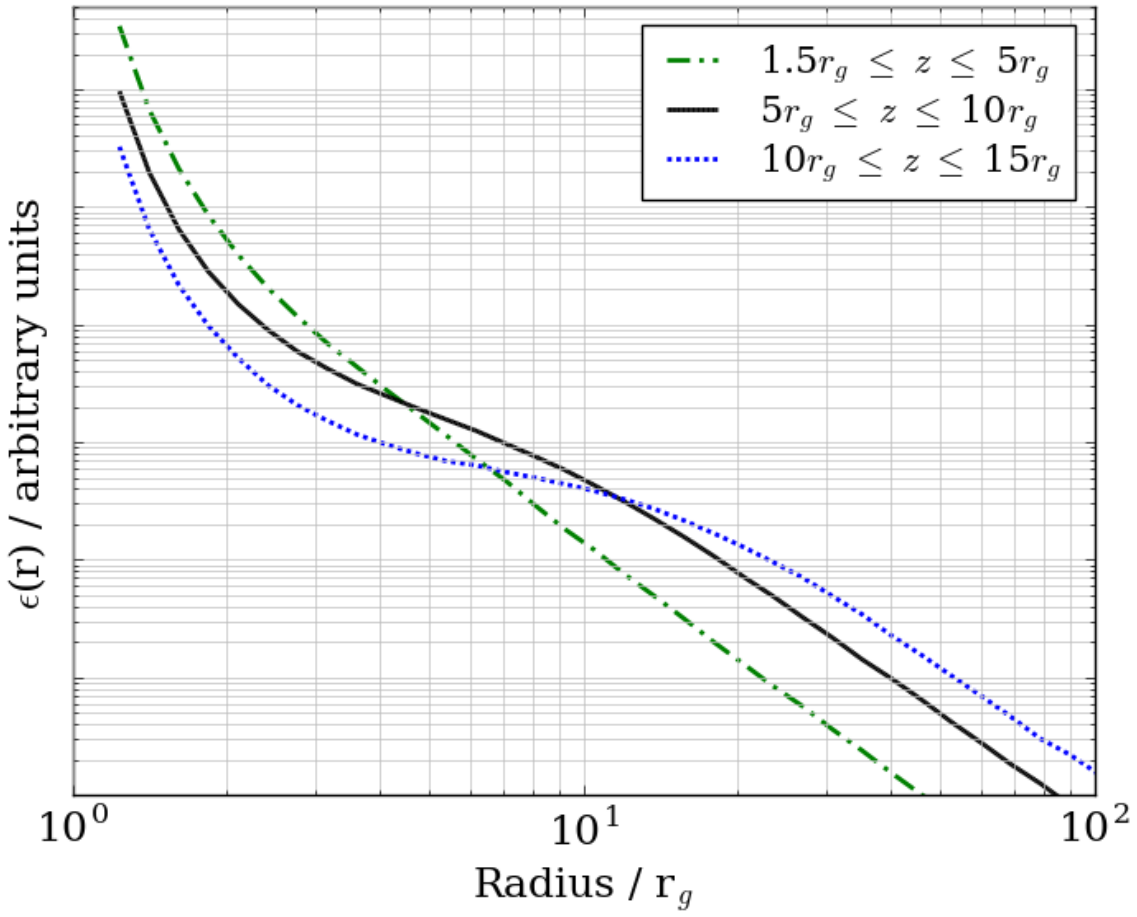

Figure 4.11: The effect of source height on the emissivity profiles of conical sources with $\psi = 10°$.

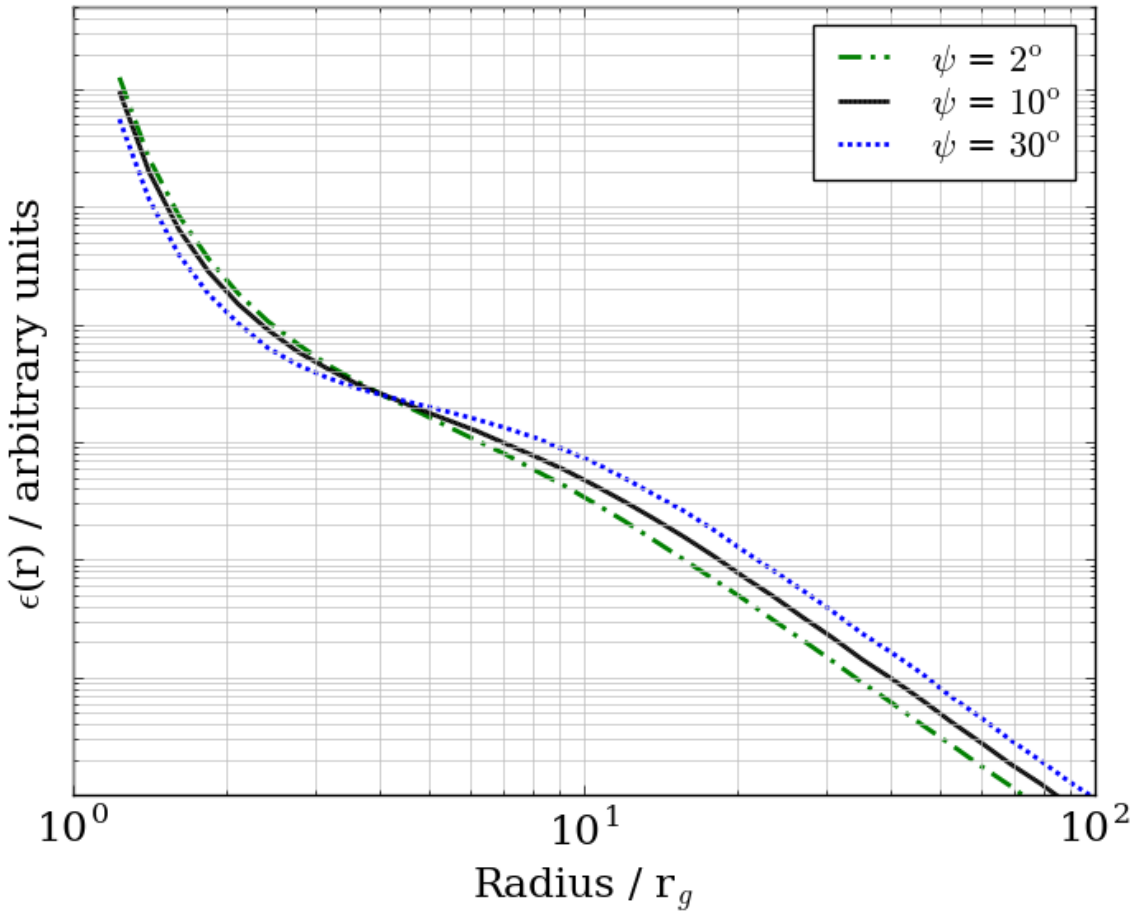

Figure 4.12: The effect of opening angle on the shape of the emissivity profile for conical sources with $\psi = 2° - 30°$ and common heights $5r_g \leq z \leq 10r_g$.

Chapter 5

Beamed Sources

Beamed sources are especially relevant in AGN where outflows or jet-like structures are present. It is therefore important and interesting to study how the emissivity profile changes due to beaming and what properties of the corona can be determined from these changes. Point source and conical geometries are the most physically plausible examples of sources that would support beaming. In such coronae, the particles that comprise the source are moving in a common direction with some velocity, changing the observed properties of the system. It is the goal of these next sections to analyse the emissivity profiles produced by such coronae and examine their differences and similarities.

5.1 Point Source

It is necessary to once again start with a simplistic point source (Figure 5.1) where the corona is located at height z above a black hole and is given a velocity radially away from

the black hole denoted henceforth as β.

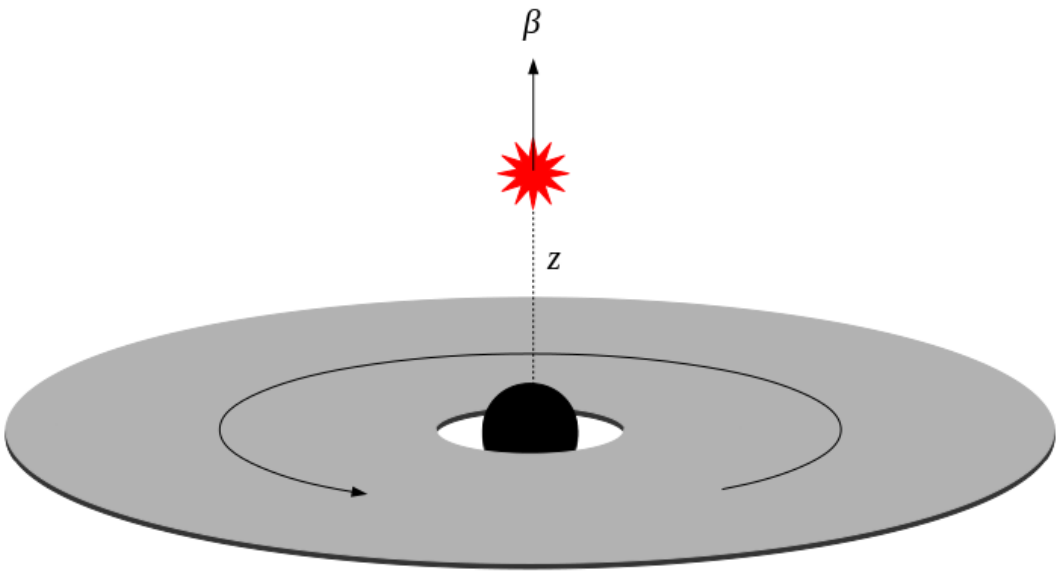

Figure 5.1: A beamed point source corona geometry with velocity β located at a height z above a rotating Kerr black hole.

In these beamed sources, only radial motion is desired and as such we must find an expression that converts the velocity from the source frame into a nearby freely falling observers frame by using $ds^2 = 0$ for photons in the Kerr metric in Boyer-Lindquist coordinates with $d\theta = d\varphi = 0$ such that (recall $c = \mu = 1$):

$$ds^2 = \left(1 - \frac{2r}{\rho^2}\right) dt^2 - \frac{\rho^2}{\Delta} dr^2 = 0 \tag{5.1}$$

From here it is possible to rearrange and solve for dr/dt, which yields:

$$\left.\frac{dr}{dt}\right|_{\text{photon}} = \frac{r^2 - 2r + a^2}{r^2 + a^2} \tag{5.2}$$

This expression for dr/dt provides the fraction of c at which the particle travels in the source frame given its velocity β according to a nearby freely falling observer. Therefore, the particle velocity in the source frame is computed as:

$$\left.\frac{dr}{dt}\right|_{\text{src}} = \beta \left.\frac{dr}{dt}\right|_{\text{photon}} \tag{5.3}$$

The value of dr/dt in the source frame is calculated at each coordinate in the geometry, in this case at one single point source, and the observed velocity β is given a direction radially outward from the black hole. With this understanding of beaming a new set of basis vectors for beamed sources is constructed:

$$\begin{aligned}
\mathbf{e}'_{(t)} &= \sqrt{\frac{1}{g_{tt} + v^2 g_{rr}}}\,(1, v, 0, 0) \\
\mathbf{e}'_{(1)} &= \sqrt{\frac{1}{g_{tt} + v^2 g_{rr}}}\left(v\sqrt{\frac{-g_{rr}}{g_{tt}}}, \sqrt{\frac{-g_{tt}}{g_{rr}}}, 0, 0\right) \\
\mathbf{e}'_{(2)} &= \left(0, 0, \sqrt{\frac{-1}{g_{\theta\theta}}}, 0\right) \\
\mathbf{e}'_{(3)} &= \sqrt{\frac{1}{g_{tt}\left(g_{\varphi t}^2 - g_{tt} g_{\varphi\varphi}\right)}}\,(g_{\varphi t}, 0, 0, -g_{tt})
\end{aligned} \tag{5.4}$$

where $\mathbf{e}'_{(t)} = \mathbf{v}$ is the four-velocity of the source moving in the r direction away from the black hole.

Using the basis vectors in Equation 5.4, a set of simulations were run for point sources with various velocities directed away from the black hole. To ensure correctness of the beaming Figure 5.2 was produced showing the distribution of initial ray momenta for a source located at $z = 5r_g$, where the magenta line represents the direction of the source velocity. As the velocity increases, the number of rays with initial momenta in the source velocity direction increases, with the case where $\beta = 0.90$ produces very few rays moving down towards the accretion disc initially.

The emissivity profiles in Figure 5.3 were calculated for point sources at $z = 10r_g$ and various β values. By increasing the velocity, fewer photons land on the inner disc while an increased number are shown to land at larger radii on the accretion disc. This result is precisely what one would expect: as β increases, photons are preferentially given a velocity in the beaming direction, therefore acting to pull ray trajectories that were sent down toward the inner disc region out to larger radii (e.g. Dauser et al. 2013).

These differences, however, are not of the same magnitude as those seen throughout Sections 3 and 4, and thus it is necessary to examine the effects of beaming more closely using the reflection fraction.

Computing R as in Equation 4.1 for a variety of point sources at different heights and with varying β values produces the results in Figure 5.4. In the case of the point source at $z = 1.5r_g$ being so close to the black hole results in most of the ray trajectories being focused on the innermost region of the disc with reflection fraction decreasing in a nearly linear fashion as the velocity is increased. For sources further away from the influence of the black hole the trend is similar as R tends to zero for $\beta = 1$ though the decreasing slope

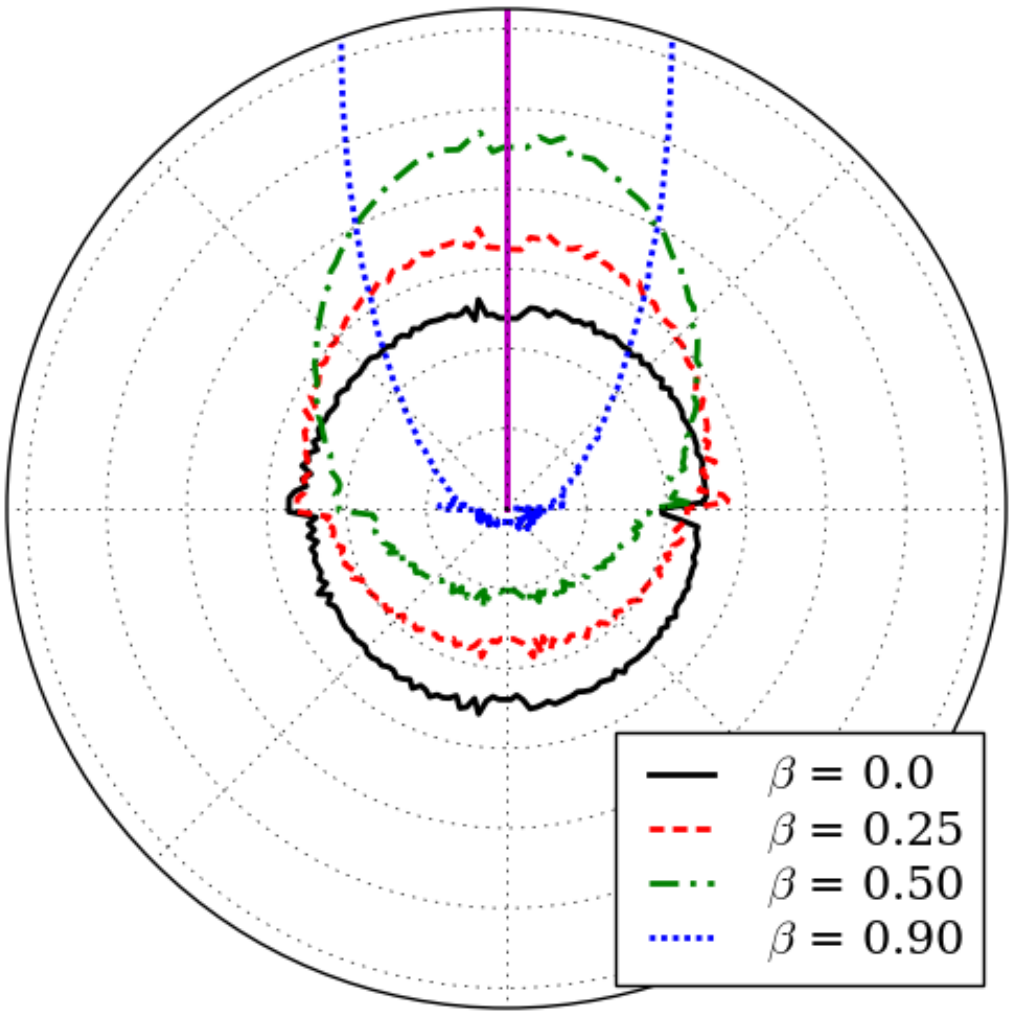

Figure 5.2: A point source at height $z = 5r_g$ with various β values showing the distribution of initial ray momenta with the magenta line representing the direction of the source velocity.

is much more shallow.

In Figure 5.5 each of the curves in Figure 5.4 has been divided by the reflection fraction of each source at $\beta = 0$ in order correct for the beaming.

Sources with $z \geq 3r_g$ exhibit corrected reflection fraction curves as a function of velocity that are very similar to each other, with those for $z \geq 5r_g$ being nearly indistinguishable.

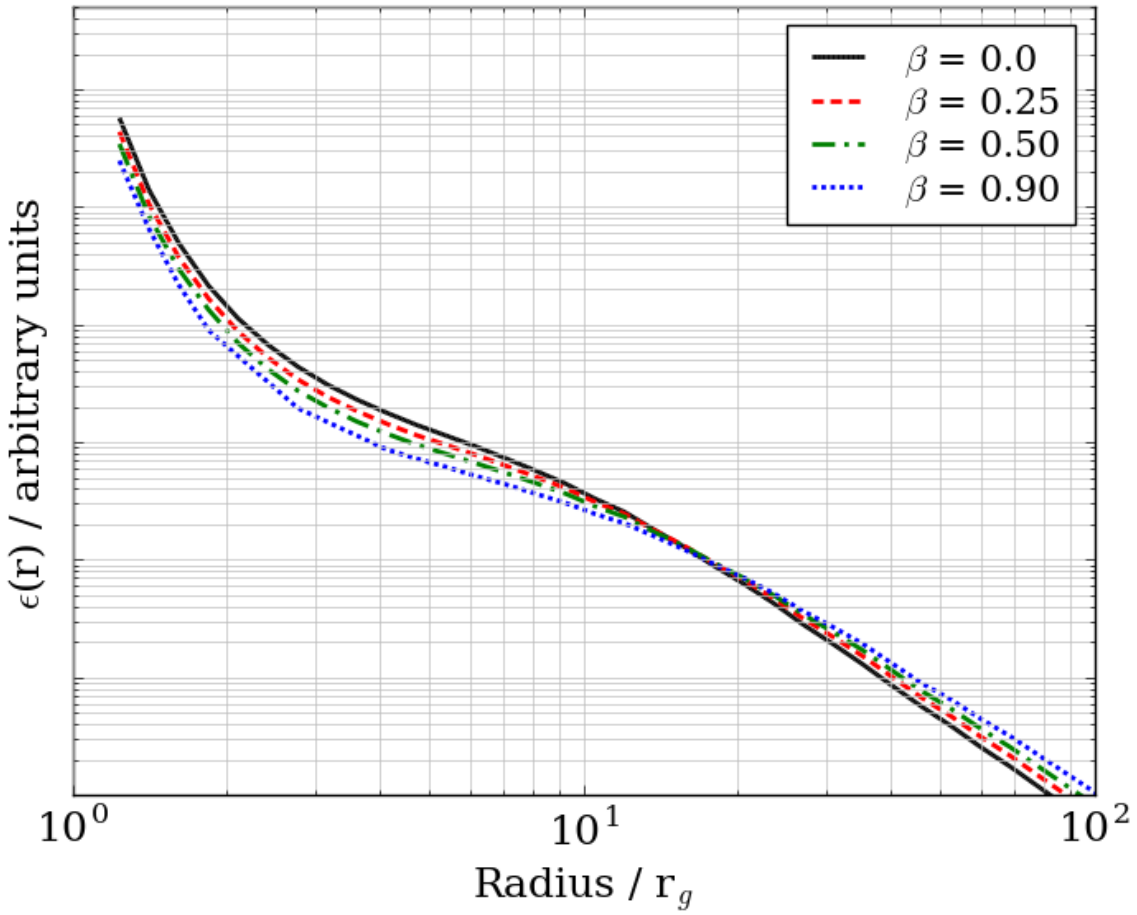

Figure 5.3: A comparison of beamed point source coronae with varying β values located a height $z = 10r_g$ above a black hole.

It is therefore possible to produce a second order polynomial fit for such sources:

$$R(\beta) \approx 0.6\beta^2 - 1.6\beta + 1 \tag{5.5}$$

which is displayed as the black solid line in Figure 5.5. The shaded grey region corresponds to curves for the minimum and maximum inclination produced by the estimation of R from Beloborodov (1999) for special relativistic cases.

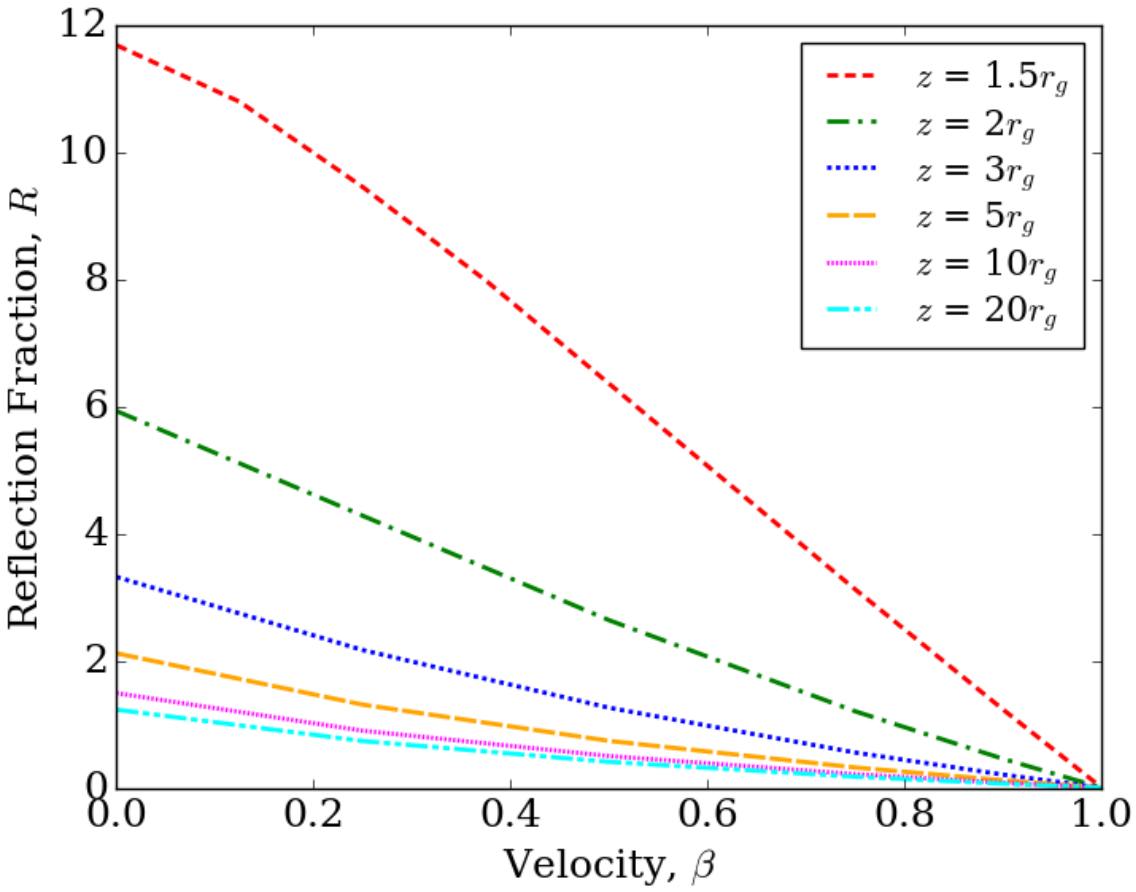

Figure 5.4: The calculated reflection fractions produced by various beamed point source coronae with varying β values and heights ranging between $z = 1.5r_g$ and $z = 20r_g$.

Figure 5.6 displays the relationship between reflection fraction and source height for stationary sources.

From this it is possible to fit a power law curve for heights $z \geq 3r_g$ to produce:

$$R(z) \approx 11.7z^{-3/2} + 1.1 \tag{5.6}$$

which is displayed as the black solid line in the plot. Combining Equations 5.5 and 5.6 we

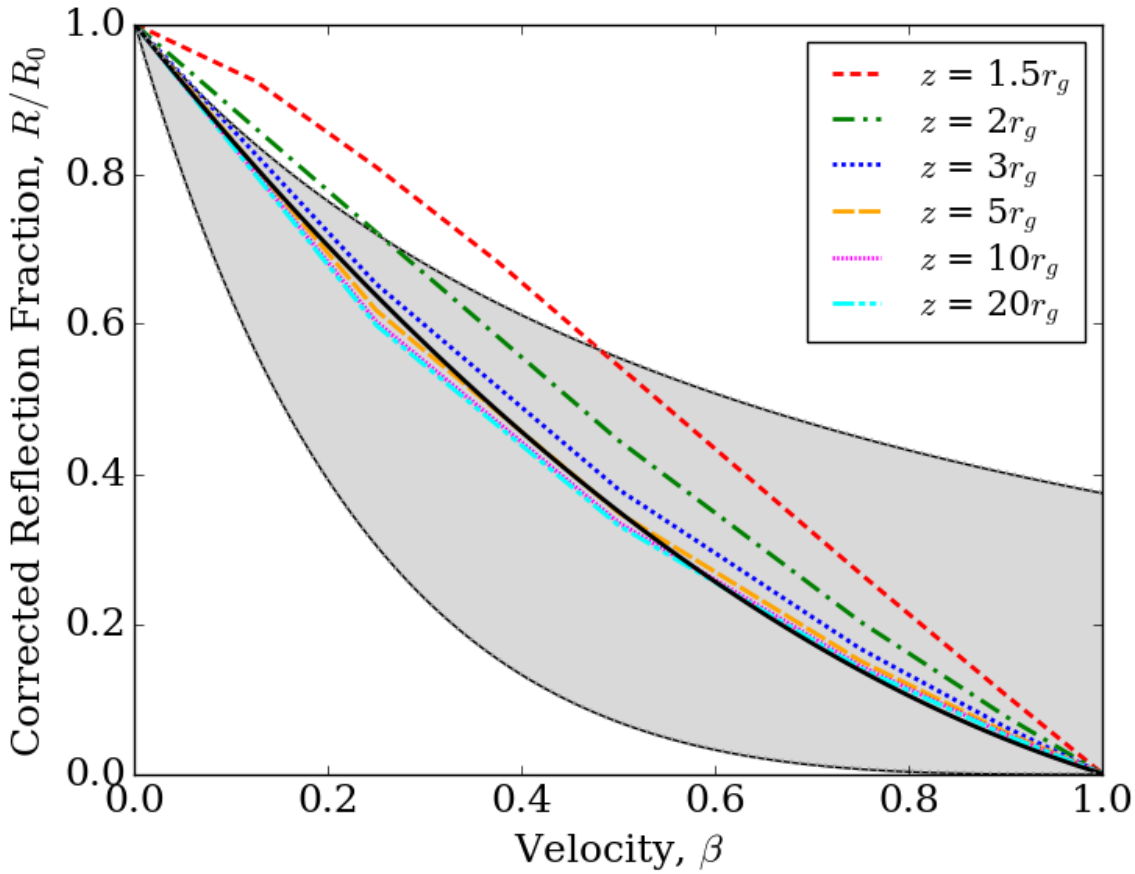

Figure 5.5: Reflection fractions for point sources between $z = 1.5r_g$ and $z = 20r_g$ normalized by the reflection fraction at $\beta = 0$ (denoted as R_0) for each source.

arrive at an expression for the measured reflection fraction as a function of the source height and velocity:

$$R(\beta, z) \approx R(\beta)\, R(z) = \left(11.7z^{-3/2} + 1.1\right)\left(0.6\beta^2 - 1.6\beta + 1\right) \tag{5.7}$$

With the height of the source known, either from the emissivity profile or time-lag analysis, and satisfying $z \geq 3r_g$ and a measured value for the reflection fraction the source velocity may be calculated via rearrangement of Equation 5.7. As aforementioned, sources closer to

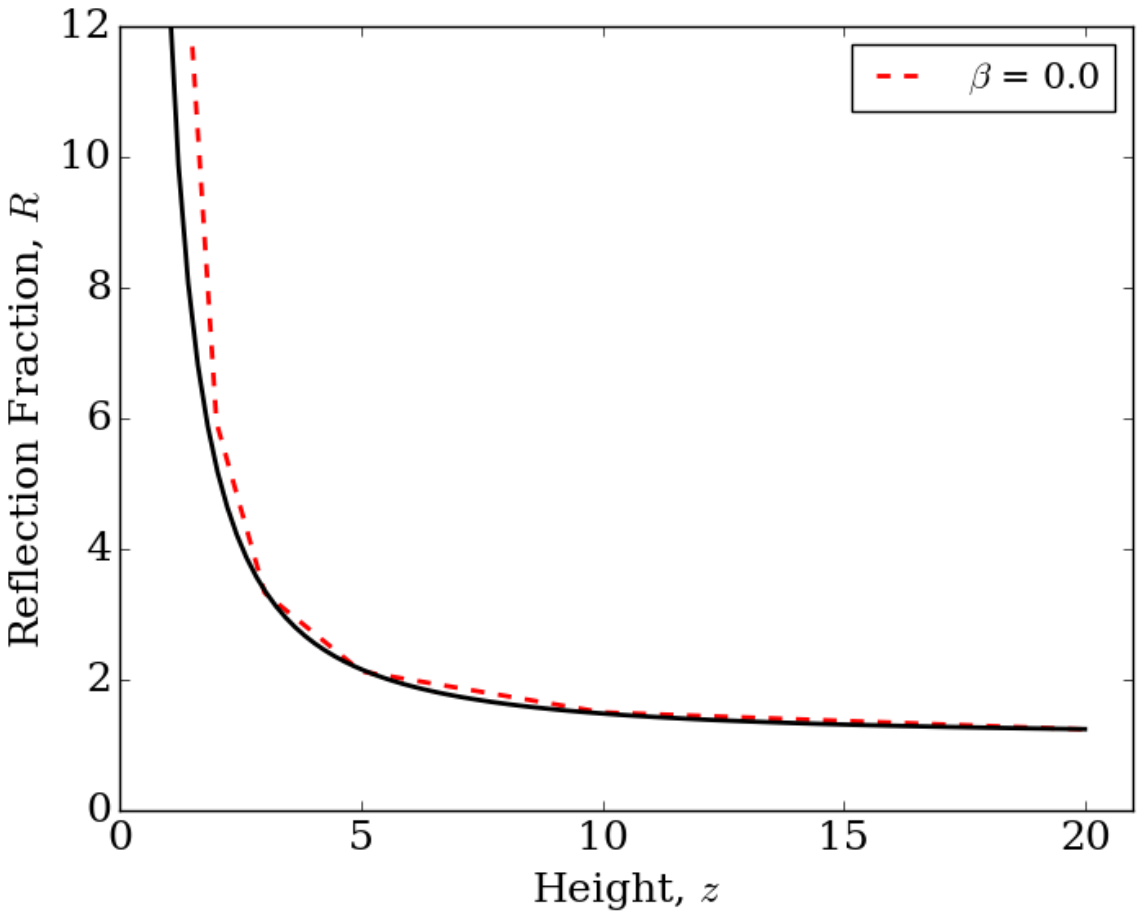

Figure 5.6: Reflection fractions for point sources between $z = 1.5r_g$ and $z = 20r_g$ with $\beta = 0$ plotted as a function of source height.

the black hole experience more extreme effects due to the strong gravity and therefore do not follow the given relationship as closely.

With this brief overview of beaming effects on point sources, more physical jet-like coronae may be studied via the simulation of beamed conical geometries.

5.2 Conical

A conical source beamed radially away from the black hole with a small opening angle is physically plausible as the jet in AGN. Figure 5.7 shows a schematic of the simulations run for beamed conical sources with a cone of height z with opening angle ψ and velocity β. It is important to note that the rest frame velocity is a constant throughout the extended geometry according to an observer. That is to say, points in the conical geometry that are nearest the black hole will have a source velocity greater than those furthest away, though due to how Equation 5.2 changes based on distance from the black hole the value of β that is observed will remain constant through the region.

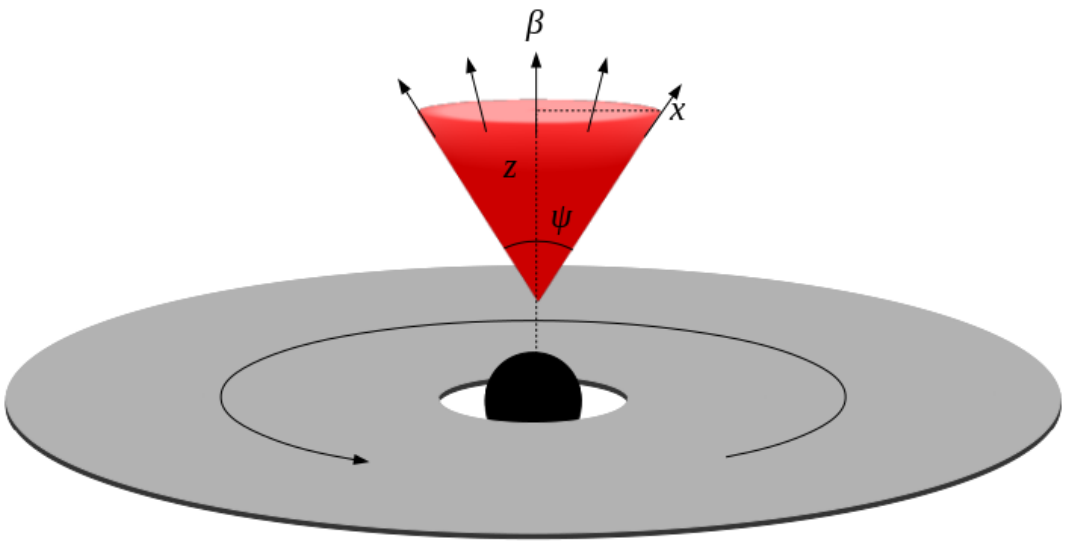

Figure 5.7: A beamed conical corona geometry with height z above a rotating Kerr black hole and opening angle ψ that extends a distance x over the accretion disc with velocity β.

Taking a conical source with $5r_g \leq z \leq 10r_g$ and $\psi = 10°$ and simulating for various

values of β produces the emissivity profiles shown in Figure 5.8. These results are consistent with those obtained in the previous section for beamed point sources. By increasing β fewer photons land on the inner portion of the accretion disc and a greater number reach larger radii. The mechanism here is also the same: ray trajectories that were originally headed down toward the accretion disc in the un-beamed case are pulled up and away for larger values of β.

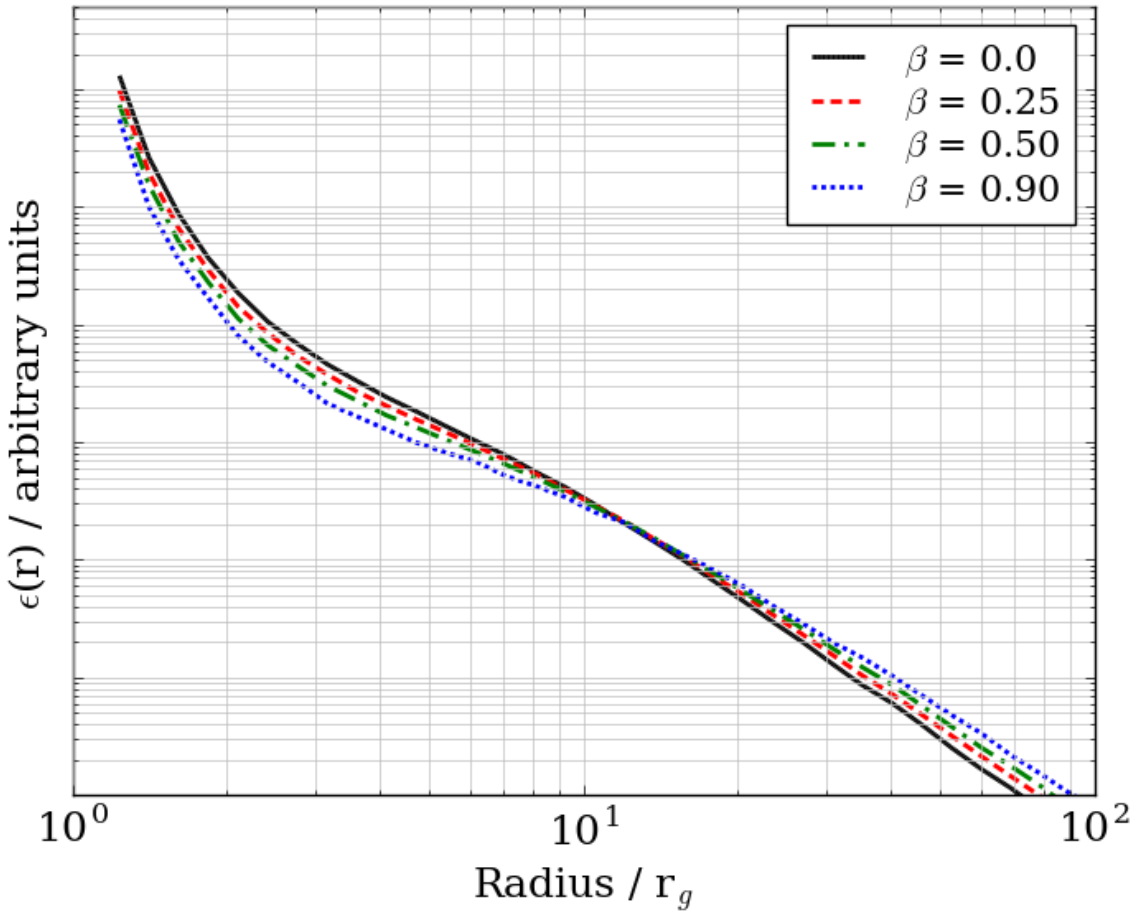

Figure 5.8: A comparison of beamed conical coronae with varying β values all with opening angle $\psi = 10°$ located a height $5r_g \leq z \leq 10r_g$ above a black hole.

Performing a similar reflection fraction analysis as with the beamed point sources pro-

duces the result shown in Figure 5.9. The trend exhibited is as expected from the previous analysis with a smoothly decreasing reflection fraction for increased value of β. Similarly to the beamed sources, close proximity to the black hole results in drop-offs in R for higher velocities while moving further away from the gravitational influence of the singularity produces smoother curves that decrease in a near linear fashion. Comparing the results in Figures 5.4 and 5.9 for point sources located at the top of each of the cones simulated reveals that the reflection fraction for conical geometries drops off more quickly than in the case of point sources. This is due to the extended nature of the cone in which the portion of the source located furthest away from the black hole emits more photons capable of escaping, lowering the reflection fraction.

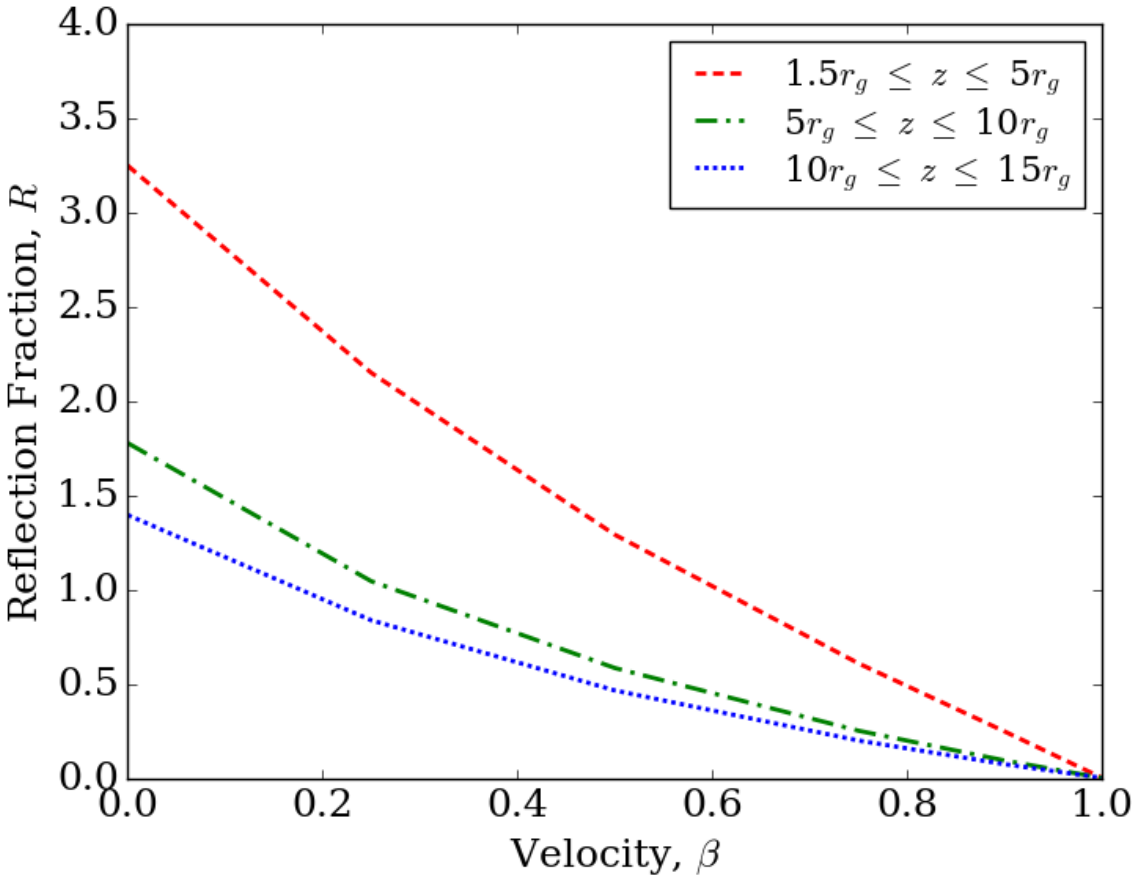

Figure 5.9: The calculated reflection fractions produced by beamed conical sources with varying β values at three different heights all with opening angle $\psi = 10°$.

Chapter 6

Modelling with XSPEC

In this section we revisit all of the corona geometries that have been covered throughout this paper in an attempt to distinguish each from the other by making use of the resulting emissivity profiles in spectral modelling. This was made possible by using the X-ray spectral fitting program XSPEC (Arnaud 1996) to produce a model composed of a power law component and a reflection spectrum using REFLIONX[1] (Ross & Fabian 2005) convolved with KDBLUR[2] to blur the spectrum in the 0.1–100 keV range. Here KDBLUR makes use of the computed values of the emissivity profiles produced through the ray tracing simulations. In addition, each of the two components were set to equal flux through the use of CFLUX[3].

For all of the models presented in this section the parameter values listed in Table 6.1 were used and held constant across each, only allowing for the values of the emissivity

[1] REFLIONX models the reflected emission produced by a power law spectrum illuminating an optically thick accretion disc of constant density.

[2] KDBLUR smooths the convolved spectrum due to relativistic effects from the accretion disc around a rotating black hole.

[3] CFLUX sets the flux of the convolved model component.

Table 6.1: Model components and their respective parameter values used to produce the spectra throughout Section 6.

Model Component	Parameter	Value
powerlaw	Photon index, Γ	2.5
kdblur	Inclination, i	60°
reflionx	Photon index, Γ	2.5
	Iron abundance / solar	5
	Ionization parameter, ξ	50 erg cm/s
cflux	Reflection fraction, R	1.0

profile to change in the KDBLUR component for the various source geometries. The range was truncated between 0.3–70 keV to show the regions of interest. Parameter values in Table 6.1 were selected to simulate a NLS1 type galaxy (like 1H 0707) with a steep photon index, moderately high iron abundance, and a strong Fe Kα line. It is important to note that only $i = 60°$ is included as this inclination provides the most variance among the spectra, allowing for a best-case scenario in being able to distinguish different source geometries.

The first step in gaining an understanding as to how the spectra change for various geometries is to examine the preliminary results of this spectral modelling for a simple point source at $z = 5r_g$ (Figure 6.1). At 6.4 keV the prominent Fe Kα line is present and broadened, as are the other lines in the spectrum, by the KDBLUR model. The broadened line exhibits a peaked blue wing and an extended red wing.

With this basic picture for our most simple model the other more complex extended geometries may now be explored. The variations between the spectra of the different sources, however, are not easily visible through the spectra alone. Therefore, for each case a ratio has been taken between two sources of similar geometry and/or size (slabs are comparable

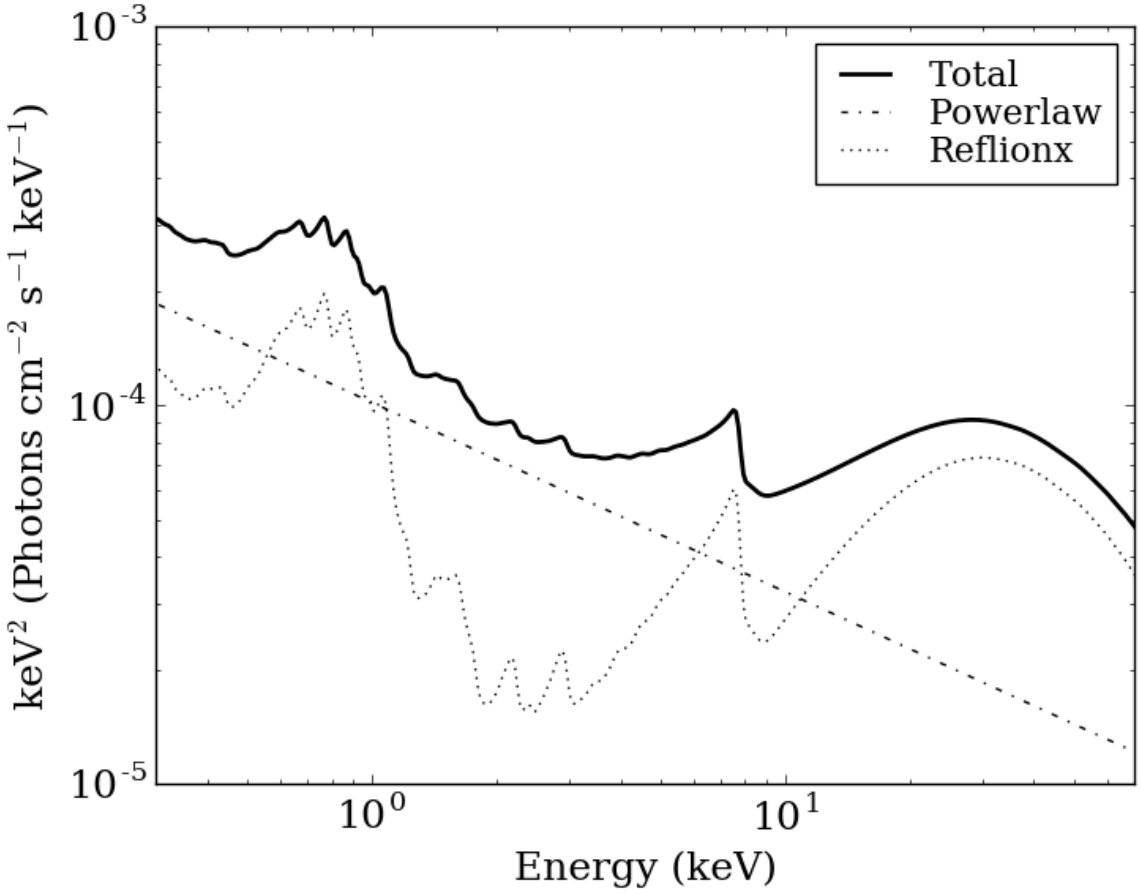

Figure 6.1: The spectrum produced by the model in Table 6.1 using the emissivity profile of a point source corona at $z = 5r_g$ on the spin axis of a rotating Kerr black hole. The reflection and power law components are made visible for completeness.

to spheroidal sources and points to cones).

These ratio plots are presented in Figures 6.2 and 6.3 where the vertical lines represent the Fe Kα line for reference (this is included in all ratio plots). In Figure 6.2 we can see that the ratio between the spheroidal corona with $R_{\rm sph} = 5r_g$ and a like sized slab geometry remains within a few per cent throughout the 0.3–70 keV range of the plot. The most notable differences are present in the blue wing of the Fe Kα line with the spheroidal source

showing a peak at energies just beyond 6.4 keV in the 7–8 keV range, though even here the differences are small.

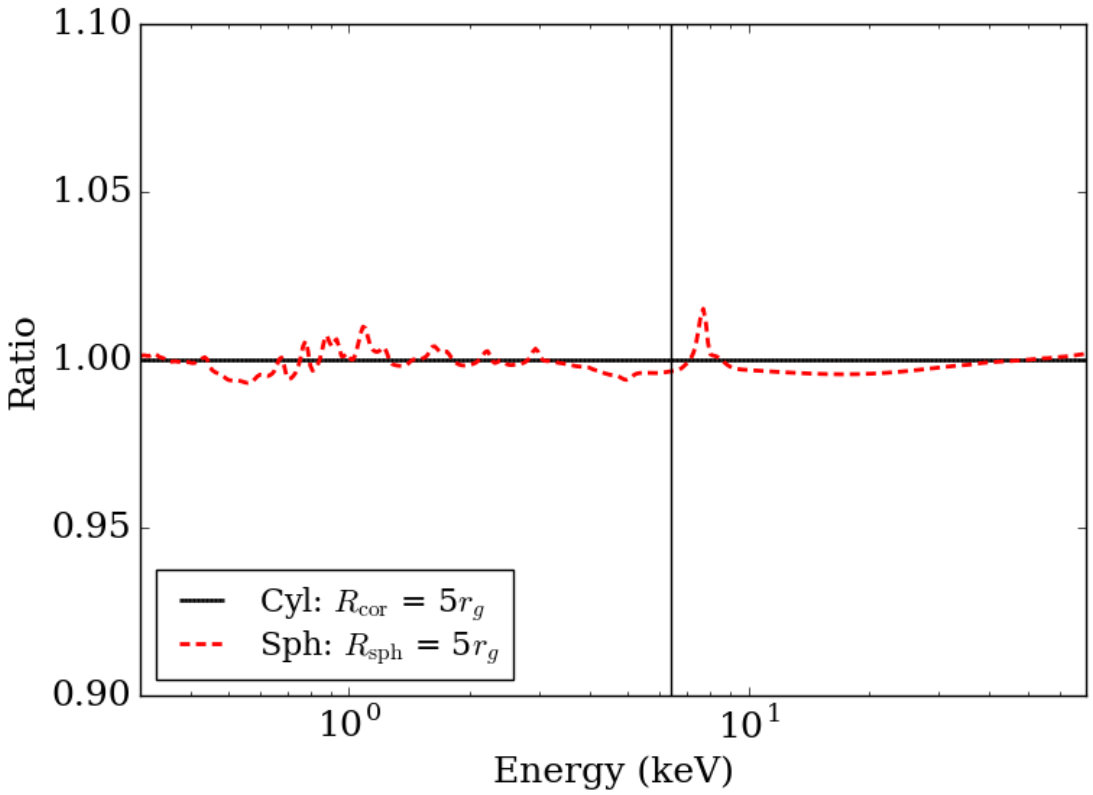

Figure 6.2: The black horizontal line denotes the ratio of the spectral model produced by a cylindrical source with itself and the red line denotes the ratio of the spectral model produced by a similar sized spheroidal source with this cylindrical geometry. The vertical line at 6.4 keV indicates the Fe Kα line for reference.

The plot shown in Figure 6.3 with the ratio taken between a conical source at $1.5r_g \leq z \leq 5r_g$ and a point source at $z = 5r_g$ shows that the spectrum produced by a conical geometry has larger ratios in the red wing of the Fe Kα line and smaller ratios in the blue wing compared to a point source at similar height, with differences over the two spectra within 5 per cent.

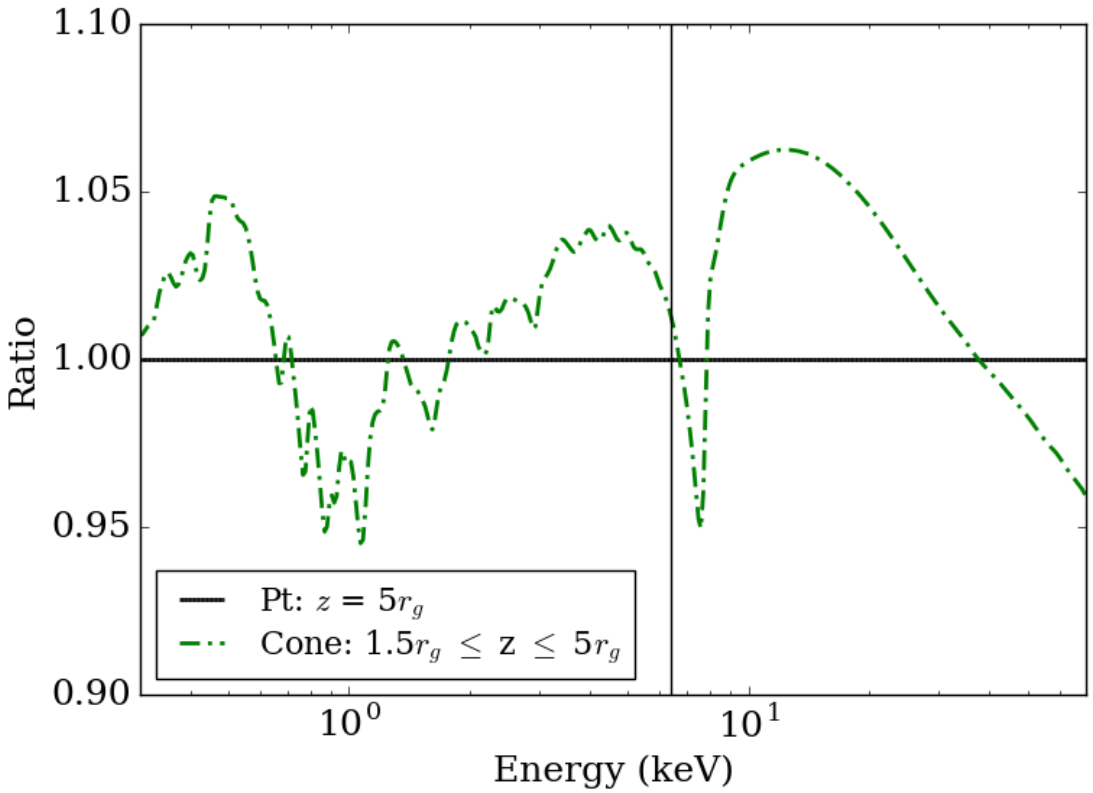

Figure 6.3: The black horizontal line denotes the ratio of the spectral model produced by a point source with itself and the green line denotes the ratio of the spectral model produced by a conical source with the point source. The vertical line at 6.4 keV indicates the Fe Kα line for reference.

Figure 6.4 presents all sources within $5r_g$ of the black hole and takes the ratio of these spectra with a point source at $z = 5r_g$. It can be seen that the point source is more similar to the conical geometry with the ratios of the slab and spheroidal geometries with the point source in the range of 10–15 per cent difference maximum.

Both Figures 6.5 and 6.6 show similar results. In the case of beamed sources versus stationary sources, the blue wing of the Fe Kα has been accentuated as a result of the beaming with a large peak in the spectrum ratios between 7–8 keV. Only the cases with the

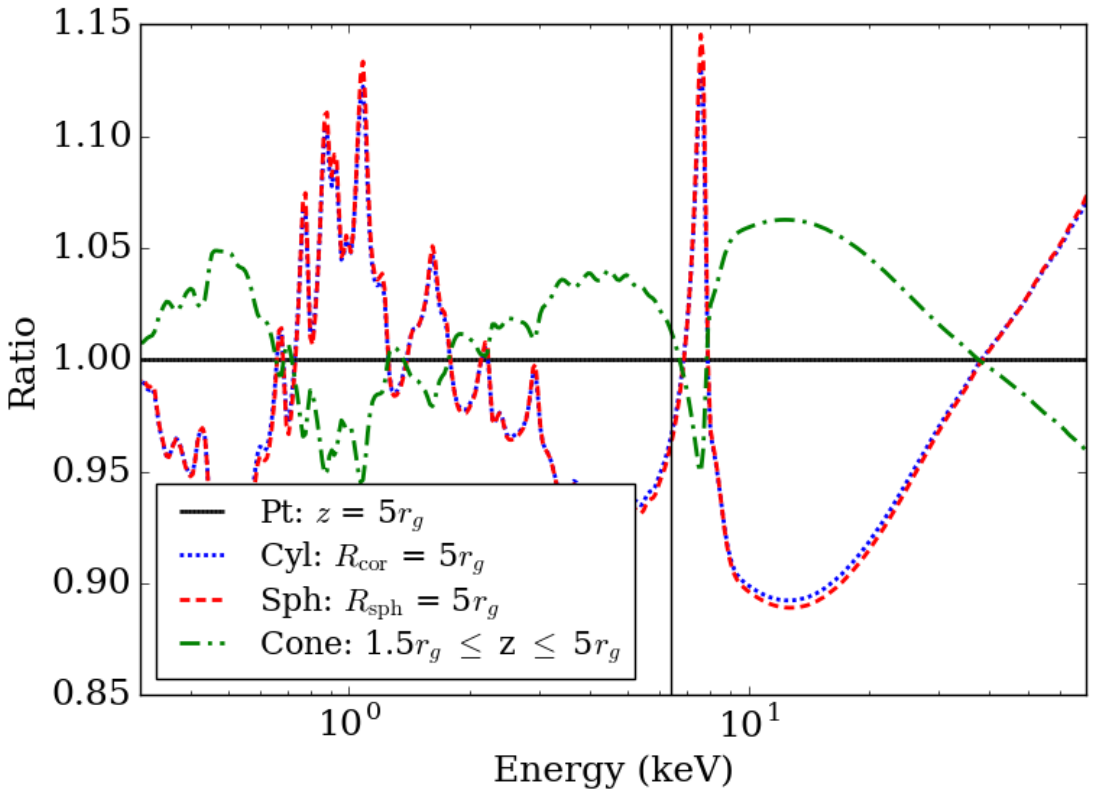

Figure 6.4: The ratios of spectral models produced by all source geometries within $5r_g$ of the black hole with a point source located at $z = 5r_g$. The black horizontal line denotes the ratio of the point source with itself with the vertical line at 6.4 keV indicating the location of the Fe Kα emission line for reference.

highest value of β show differences in the ratios in the range of 5–10 per cent.

Simulations of spectral data, as it would be measured by *XMM-Newton*, were performed based on extreme objects with properties given in Table 6.1 that are bright (2–10 keV flux $\sim 10^{-11}$ erg/cm^2/s) and observed over long exposure times (e.g. 100 kiloseconds) to produce good quality spectra. For such sources the geometries are distinguishable from each other, as shown by the ratio plot in Figure 6.7. This solution may not be unique from other interpretations of the AGN spectrum (e.g. partial covering or multiple Comptonising

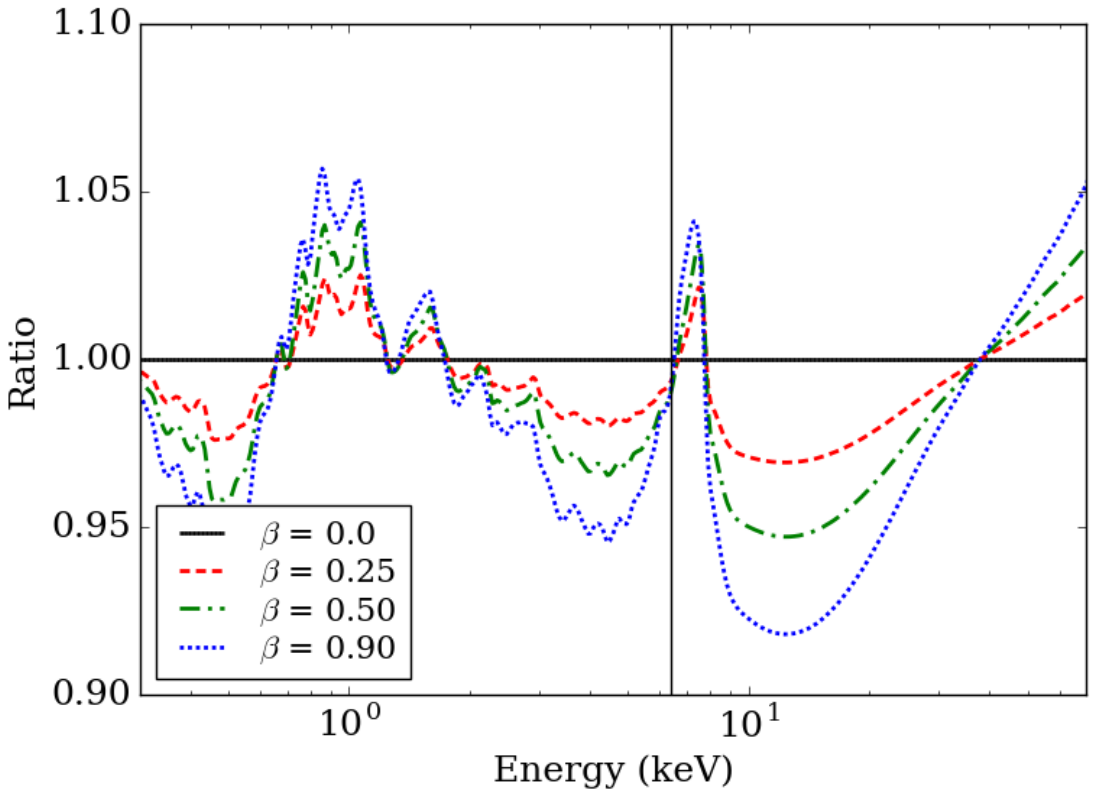

Figure 6.5: The ratios between the spectral models produced by a stationary point source at $z = 5r_g$ and beamed point sources at the same height with varying values of β. The vertical line at 6.4 keV indicates the Fe Kα line for reference.

layers), but it suggests that current data could distinguish between different geometries.

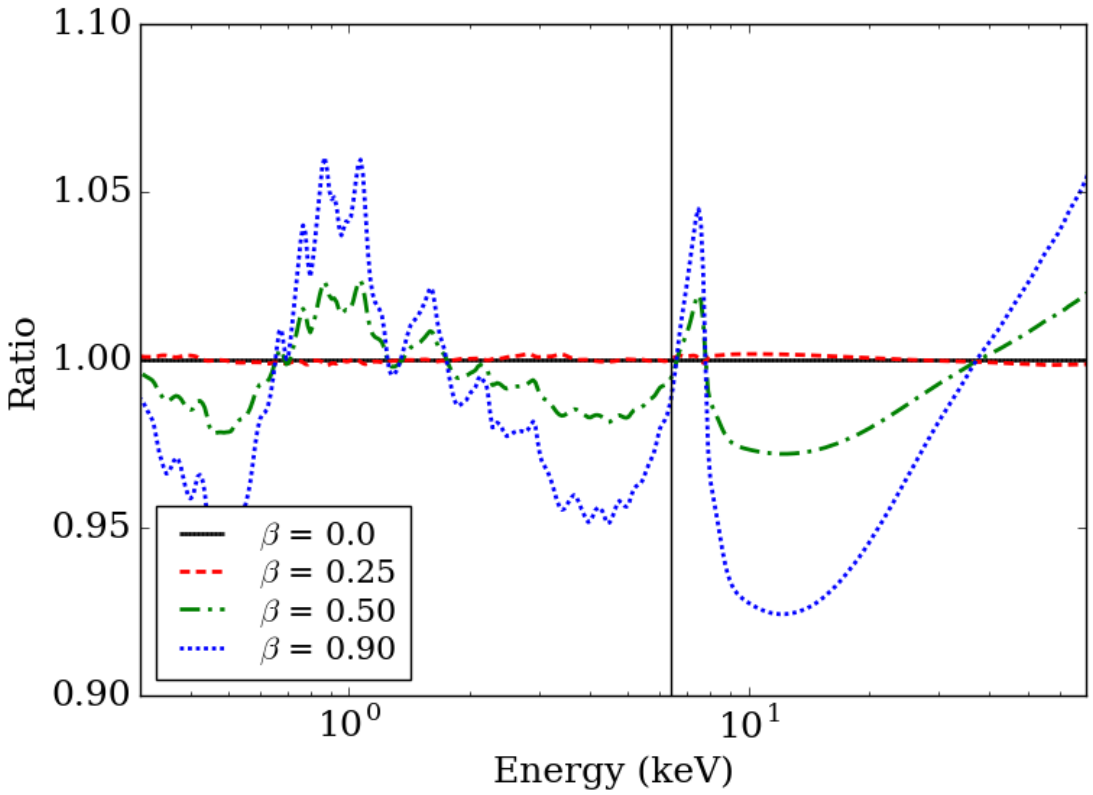

Figure 6.6: The ratios between the spectral models produced by a stationary conical source at $1.5r_g \leq z \leq 5r_g$ and beamed conical sources at the same height with varying values of β. The vertical line at 6.4 keV indicates the Fe Kα line for reference.

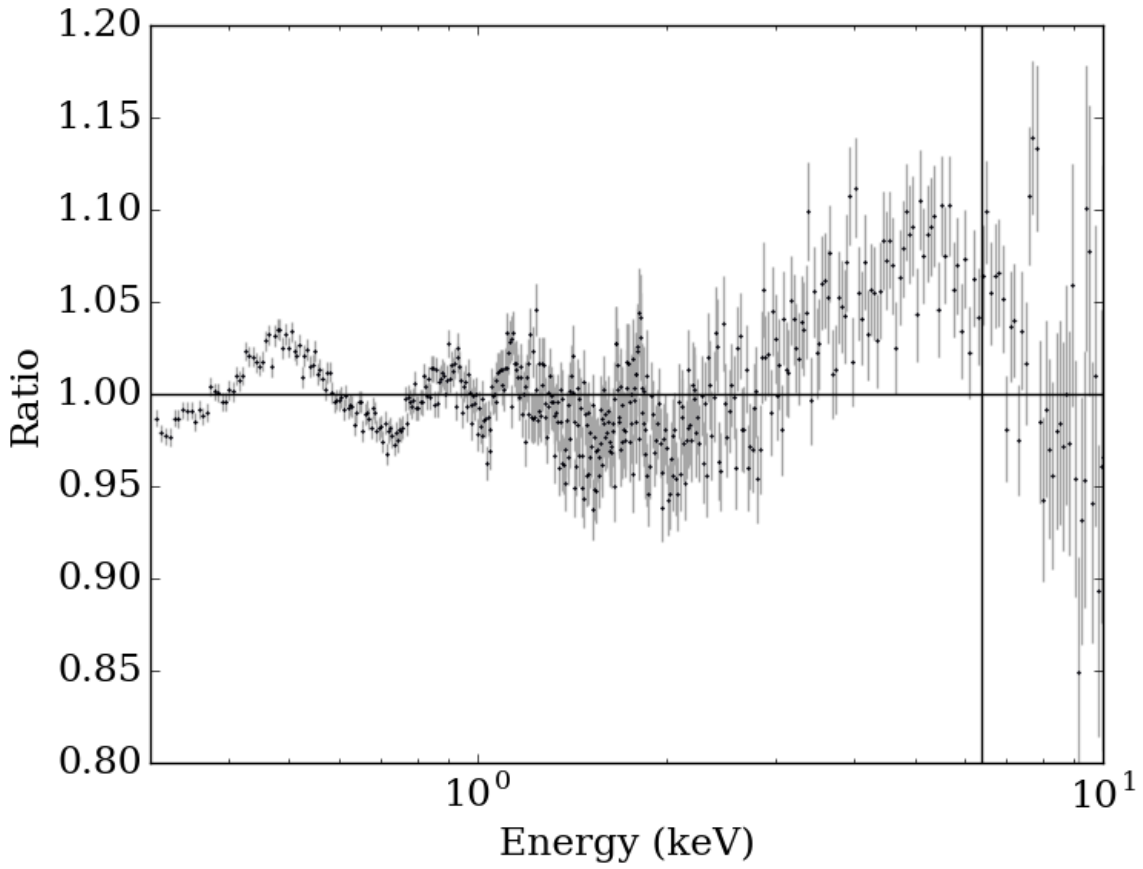

Figure 6.7: The ratio of a simulated spectrum produced by a point source corona at $z = 5r_g$ to the spectral model of a spherical geometry of radius $R_{\rm sph} = 5r_g$ located on the accretion disc. The spheroidal model has been fit to the simulated data produced by the point source.

Chapter 7

Discussion

The emissivity profiles obtained via ray tracing simulations as well as the spectral modelling of point sources and extended corona geometries provide insight into the differences and similarities between the four geometries studied. In all of the emissivity profiles calculated a twice-broken power law shape is observed with steep slope at low radii, flattened midsection, and outer profile slope dropping off as r^{-3} . After simulating and confirming the results of simple "lamppost" point source models a series of three extended geometries were studied by varying a number of parameters.

The height of the source above the black hole was found to cause the greatest difference in profile shape for point source and conical geometries (Figures 3.2 and 4.11) while being less significant the radially extended geometries (Figures 4.3, 4.6). In all cases increased height caused the midsection of the profile to flatten further and accentuate the twice-broken shape of the profile described in WF12.

Horizontal displacement from the spin axis for point sources (Figure 3.3) and radial

extent over the accretion disc for conical geometries (Figure 4.12) also produced notable profile differences though the results here were much less distinct than for vertical height. In the case of cylindrical and spheroidal sources radial extent had a greater effect on the profile shape (Figures 4.4 and 4.6) being a more significant parameter than the height of such sources. For geometries with more total coverage over the accretion disc the break in the emissivity profiles shifted to larger radii, effectively tracing the edge of the extended source.

While being able to tell what properties a particular geometry possesses it is perhaps more interesting to study the differences between the various sources simulated. Comparing the emissivity profiles produced by the four different geometries found that point sources can be distinguished from extended geometries such as cylindrical slabs and spheroidal clouds.

Cylindrical and spheroidal geometries were found to produce very similar emissivity profiles with minute differences (Figure 4.6). Comparisons between spheroidal and ellipsoidal sources found no significant differences between the two to allow for any true differentiation.

The same can be said about the differences between point source and conical geometries with narrow opening angles. In the case of conical sources with narrow opening angles the emissivity profile alone is insufficient in determining whether the parent source geometry is a point or cone (Figure 4.10). These results suggest that radial extent and coverage over the accretion disc are more impactful on the resulting emissivity profile than vertical extent perpendicular to the disc.

However, differences between point source and conical geometries arise once reflection fraction is considered, with the conical source exhibiting a larger reflection fraction in all

cases than the equivalent point source. This is as expected due to the extended nature of the cone, allowing more photons to be emitted nearer the black hole than a point source located at the top of the cone, resulting in fewer photons being able to escape the system and more being reflected off of the accretion disc.

In the analysis of beamed point source and conical geometries, which were given a velocity β directed radially away from the black hole, the emissivity profiles in both cases exhibit a common trend: flattening of the profile midsection with increased β (Figures 5.3 and 5.8). The profiles for the various β values are all very similar to each other, and thus it is again necessary to explore the reflection fraction. Changes in R for point source and conical geometries follow an expected trend of decreasing to zero with a shallow slope as β approaches the limit of light speed, with the exception being the point source located closest to the black hole (Figure 5.4 and 5.9). An estimation of the measured reflection fraction in Equation 5.7 was produced by fitting the curves with $z \geq 3r_g$ in Figure 5.5 with a second order polynomial (Equation 5.5) and in Figure 5.6 with a power law (Equation 5.6). With the height of the point source known, from an analysis of the emissivity profile or through time-lag studies, and the reflection fraction measured from AGN data it is possible to rearrange Equation 5.7 and estimate the source velocity.

In Section 1 it was discussed that the illumination profile (photons incident on the disc) and emissivity profile (photons processed and re-emitted by the disc) were to be used interchangeably throughout this work. The equivalency assumed, however, may not be exactly true due to various factors including the absorption and emission processes in the disc that are affected by ionisation gradient across the surface of the accretion disc which

contribute to differences between the illumination and emissivity profile. For example, Svoboda et al. (2012) show the effects of ionisation gradient on the emissivity profile. In this work we were interested in emissivity profiles as measured from the Fe Kα emission line and assumed that the line flux is proportional to the incident flux upon the disc with no other factor (e.g. ionisation gradient) causing variation in the emitted line flux between different radii.

Using the computed emissivity profiles it is possible to simulate spectra using XSPEC to explore the feasibility of distinguishing the different geometries in observational AGN spectral data. Modelling in XSPEC was done using a combination of power law and blurred reflection models. This model was used to create a spectrum for each corona geometry that could then be compared with the spectrum of another geometry in an effort to examine differences between them (Figures 6.2, 6.3, & 6.4).

With this technique it can be seen that the largest differences between the spectra occurs around the Fe Kα line at 6.4 keV. Figure 6.4 shows that in a comparison of all geometries to a point source the differences are less than 15 per cent, with cylindrical and spheroidal sources being most different. Performing the same analysis with beamed point sources and conical geometries finds that differences between the spectra are about 5–10 per cent when comparing a stationary source to beamed sources of the same geometry.

The results found throughout Section 6 suggest moderate differences in the spectra for the various geometries studied. The differences require high quality data from current missions observing extreme, bright sources over long exposure times to be distinguishable. The solution found here may not be unique as other model interpretations could result in

good fits. Athena-like missions with large collecting area (e.g. Nandra et al. 2013) or those that are Hitomi-like with high spectral resolution (e.g. Takahashi et al. 2014) will provide the ability to more finely discern the differences between the geometries.

All of the results obtained throughout this study of various corona geometries suggest that emissivity profiles are a useful tool in determining different sources, but that they are also part of a larger tool-kit. The corona geometry itself is an important indicator of the formation processes that take place to create the X-ray source in AGN, processes which are still not fully understood. Parameters such as the extent of the source over the accretion disc are readily identified through the analysis of the emissivity profile. In order to precisely identify the geometry of a specific source emissivity profiles must be used in conjunction with studies in reflection fraction, time lag analysis, and spectral modelling. Beaming, for example, proved to have a lesser effect on the emissivity profile than did extent over the disc, requiring an analysis of reflection fraction in order to determine the effect of source velocity.

Chapter 8

Conclusions

Through general relativistic ray tracing simulations of various coronal geometries it was found that point sources can be distinguished from extended geometries such as cylindrical slabs and spheroidal clouds through the differences in the emissivity profiles alone. In the case of conical geometries it was found that the emissivity profiles produced were too similar to point sources to be distinguished via profiles alone, and thus an analysis of reflection fraction was necessary in order to differentiate the two geometries.

In the case of beamed point sources and conical coronae it was again necessary to use reflection fraction in order to determine the differences between beamed geometries as the emissivity profiles were not significantly different from each other. By fitting reflection fraction curves as a function of source velocity and height it was possible to produce an estimate of the point source reflection fraction given velocity and height of the corona.

Using XSPEC to simulate spectra for the different geometries it was found that differences in the simulated spectra did not exceed 15 per cent even in the most extreme cases among

the different geometries. Simulated data suggest that differences between the emissivity profiles of the various geometries can be detected in high quality data for extreme, bright sources over long exposures in current data.

The results presented in this work all suggest that a collective tool-kit involving several analysis techniques (e.g. emissivity profiles, reflection fraction, time lag analysis, and spectral modelling) are required in order to determine the true geometry of the corona.

Bibliography

Antonucci, R. 1993, ARA&A , 31, 473

Antonucci, R. R. J. & Miller, J. S. 1985, ApJ , 297, 621

Arnaud, K. A. 1996, in Astronomical Society of the Pacific Conference Series, Vol. 101, Astronomical Data Analysis Software and Systems V, ed. G. H. Jacoby & J. Barnes, 17

Beloborodov, A. M. 1999, ApJ , 510, L123

Blandford, R. D. & Znajek, R. L. 1977, MNRAS , 179, 433

Brenneman, L. W. & Reynolds, C. S. 2006, ApJ , 652, 1028

Crummy, J., Fabian, A. C., Gallo, L., & Ross, R. R. 2006, MNRAS , 365, 1067

Dauser, T., Garcia, J., Wilms, J., et al. 2013, MNRAS , 430, 1694

Dovciak, M., Svoboda, J., Goosmann, R. W., et al. 2014, ArXiv e-prints

Fabian, A. C., Kara, E., Walton, D. J., et al. 2013, MNRAS , 429, 2917

Fabian, A. C., Rees, M. J., Stella, L., & White, N. E. 1989, MNRAS , 238, 729

Fabian, A. C., Zoghbi, A., Ross, R. R., et al. 2009, Nature , 459, 540

Falcke, H. & Biermann, P. L. 1995, A&A , 293

Galeev, A. A., Rosner, R., & Vaiana, G. S. 1979, ApJ , 229, 318

Gallo, L. C. 2011, JRASC , 105, 143

Gallo, L. C., Fabian, A. C., Grupe, D., et al. 2013, MNRAS , 428, 1191

Gallo, L. C., Wilkins, D. R., Bonson, K., et al. 2015, MNRAS , 446, 633

Ghez, A. M., Becklin, E., Duchjne, G., et al. 2003, Astronomische Nachrichten Supplement, 324, 527

Ghisellini, G., Haardt, F., & Matt, G. 2004, A&A , 413, 535

Gierliński, M. & Done, C. 2004, MNRAS , 349, L7

Haardt, F. & Maraschi, L. 1991, ApJ , 380, L51

Koratkar, A. & Blaes, O. 1999, PASP , 111, 1

Laor, A. 1991, ApJ , 376, 90

Malkan, M. A. & Sargent, W. L. W. 1982, ApJ , 254, 22

Merloni, A. & Fabian, A. C. 2001, MNRAS , 328, 958

Miniutti, G., Fabian, A. C., Goyder, R., & Lasenby, A. N. 2003, MNRAS , 344, L22

Murray, N. & Chiang, J. 1997, ApJ , 474, 91

Nandra, K., Barret, D., Barcons, X., et al. 2013, ArXiv e-prints

Parker, M. L., Tomsick, J. A., Miller, J. M., et al. 2015, ApJ , 808, 9

Peterson, B. M. 1997, An Introduction to Active Galactic Nuclei (Cambridge University Press)

Porquet, D., Reeves, J. N., O'Brien, P., & Brinkmann, W. 2004, A&A , 422, 85

Reynolds, C. S. & Nowak, M. A. 2003, Phys. Rep. , 377, 389

Ross, R. R. & Fabian, A. C. 1993, MNRAS , 261, 74

Ross, R. R. & Fabian, A. C. 2005, MNRAS , 358, 211

Schödel, R., Ott, T., Genzel, R., et al. 2002, Nature , 419, 694

Seyfert, C. K. 1943, ApJ , 97, 28

Shakura, N. I. & Sunyaev, R. A. 1973, A&A , 24, 337

Suebsuwong, T., Malzac, J., Jourdain, E., & Marcowith, A. 2006, A&A , 453, 773

Svoboda, J., Dovčiak, M., Goosmann, R. W., et al. 2012, A&A , 545, A106

Takahashi, T., Mitsuda, K., Kelley, R., et al. 2014, Proc. SPIE , 9144, 914425

Torres, D. F. 2003, ArXiv Astrophysics e-prints

Urry, C. M. & Padovani, P. 1995, PASP , 107, 803

Wilkins, D. R. 2015, in The Extremes of Black Hole Accretion, 66

Wilkins, D. R. & Fabian, A. C. 2011, MNRAS , 414, 1269

Wilkins, D. R. & Fabian, A. C. 2012, MNRAS , 424, 1284

Wilkins, D. R. & Fabian, A. C. 2013, MNRAS , 430, 247

Wilkins, D. R. & Gallo, L. C. 2015a, MNRAS , 449, 129

Wilkins, D. R. & Gallo, L. C. 2015b, MNRAS , 448, 703

Wilkins, D. R., Gallo, L. C., Grupe, D., et al. 2015, MNRAS , 454, 4440

Wilkins, D. R., Kara, E., Fabian, A. C., & Gallo, L. C. 2014, MNRAS , 443, 2746

Zoghbi, A., Fabian, A. C., Uttley, P., et al. 2010, MNRAS , 401, 2419